Verification of a Finite Element Model for Pyrolyzing Ablative Materials

Timothy K. Risch[1]
NASA Armstrong Flight Research Center, Edwards, CA 93523

Ablating thermal protection system materials have been used in many reentering spacecraft and in other applications such as rocket nozzle linings, fire protection materials, and as countermeasures for directed-energy weapons. The introduction of the finite element model to the analysis of ablation has arguably resulted in improved computational capabilities due to the flexibility and extended applicability of the method, especially to complex geometries. Commercial finite element codes often provide enhanced capabilities over custom, specially-written programs, such as versatility, usability, pre- and post-processing, grid generation, total life-cycle costs, technical support, maintenance, and speed. Computed results for several test problems using the commercial finite element code COMSOL Multiphysics® (COMSOL, Inc. Burlington, Massachusetts) are compared to predictions generated from other computational tools including the Fully Implicit Ablation and Thermal (FIAT) Response code. The results obtained from COMSOL Multiphysics® compare favorably with other methods and demonstrate that COMSOL Multiphysics® is an accurate and advantageous tool for the analysis of pyrolyzing ablators.

Nomenclature

Latin

A = cross-sectional area, m^2 or pre-exponential factor, 1/s
B_{ss} = ratio of char to pyrolysis mass loss at steady-state
B' = normalized mass transfer rate, $\dot{m}/\rho_e u_e C_M$
C = radiation intensity profile constant
C_H = Stanton number for heat transfer
C_M = Stanton number for mass transfer
C_p = specific heat at constant pressure, J/kg-K
E = activation energy, J/mol
F = radiation view factor
FIAT = Fully Implicit Ablation and Thermal Response code
h = enthalpy, J/kg, or heat transfer coefficient, W/m^2-K
$\bar{h}$ = enthalpy defined as $(\rho_v h_v(T) - \rho_c h_c(T))/(\rho_v - \rho_c)$, J/kg
I = incident surface radiation, W/m^2
k = thermal conductivity, W/m-K
$\dot{m}$ = surface mass loss rate, kg/m^2-s
p = pressure, atm
q = heat flux, W/m^2
r = radial position, m
R = universal gas constant, 8.314 J/mol-K
$\dot{s}$ = surface recession rate, m/s
SSEB = steady-state energy balance
t = time, s
T = temperature, K
TACOT = Theoretical Ablative Composite for Open Testing
TPS = thermal protection system

[1] Deputy Branch Chief, Aerostructures Branch, MS 4820-2A, P.O. Box 273, Edwards, CA 93523

u = velocity, m/s
x = axial coordinate fixed in space, m or mass fraction of pure virgin material
y = axial coordinate tied to the receding surface, m

Greek

α = thermal diffusivity, m^2/s or surface absorptivity
β = heating rate, K/s
ε = surface emissivity or error in non-linear equations
Γ = resin volume fraction
λ = blowing reduction factor
ρ = density, kg/m^3
$\rho_e u_e C_H$ = heat transfer coefficient, kg/m^2-s
$\rho_e u_e C_M$ = mass transfer coefficient, kg/m^2-s
ψ = decomposition exponent
σ = Stefan-Boltzmann constant, 5.6704×10^{-8} W/m^2-K^4
ϕ = void fraction
Φ = potential function

Subscripts

A = material component 1, resin
B = material component 2, resin
C = material component 3, reinforcement
b = backface
c = char
e = freestream
g = pyrolysis gas
i = material number
r = recovery
s = surface
v = virgin
w = wall
∞ = background condition
0 = reference condition

I. Introduction

Ablating thermal protection system (TPS) materials have been used in many reentering spacecraft and for other applications such as rocket nozzle linings, fire protection materials, and as countermeasures for directed-energy weapons. Ablative TPS materials are being developed for the future Orion capsule.

Ablative materials can be divided into two basic groups: pyrolyzing and non-pyrolyzing. Pyrolyzing materials are those that decompose in-depth due to heat conduction away from the heated surface and develop a residual char. The in-depth decomposition generates gases that percolate up through the material to the surface, absorbing energy. Vaporization and chemical reactions at the surface absorb energy, reducing the heat that travels into the material. The gas generated in-depth and at the surface due to vaporization then enters the boundary layer and reduces the convective heat transfer due to the gas flow transverse to main surface flow. Non-pyrolyzing materials, on the other hand, do not generate gas in-depth, but only at the surface. Non-pyrolyzing ablators are a subset of pyrolyzing materials and can be analyzed using the same tools.

In the early 1960s, Kendall, et al. at the Aerotherm Corporation (Palo Alto, California)[1] developed a finite-difference model for the one-dimensional, in-depth heat transfer and thermal decomposition for pyrolyzing, ablative materials. They created the Charring Material Ablation (CMA) program, which is still used today. Subsequently, the framework was extended to two-dimensional, axi-symmetric geometries.[2] Since then, a number of researchers have developed new and improved programs for the analysis of pyrolyzing ablation based on the original fundamental physical assumptions of the original Aerotherm model.[3-10]

The introduction of the finite element model to the analysis of ablation has arguably resulted in improved computational capabilities due to the flexibility and enhanced applicability of the method, especially to complex geometries. Several custom-written programs have demonstrated the capability of the finite element method[11-14] applicable to ablation problems. Other ablation programs have utilized general-purpose finite element libraries[15,16] as a way to leverage existing computational capabilities. Recent improvements in the computational capabilities of

general, commercial finite element programs have allowed these codes to be used for the analysis of ablation with a perceived user benefit.[17-23]

There are numerous advantages to using a commercial finite element code for the analysis of physical phenomenon. Much of the structural and computational fluid dynamics analysis and design work is now performed using commercial codes as opposed to custom-written codes, because commercial codes provide enhanced capability in the form of usability, pre- and post-processing, built-in grid generation, speed, life cycle cost, technical support, maintenance, and flexibility. Commercial codes also are utilized by a very large number of users, which contributes to the robustness and accuracy of the codes and aids the refinement of the codes by way of application to diverse problems. Finally, many commercial codes also possess the capability to perform coupled analysis, including structural and electromagnetic physics in parallel with the thermal/ablation analysis.

The thermal analysis of non-pyrolyzing ablative materials requires the following computational capabilities:

- Solid, non-linear heat conduction with the capability to employ thermal and transport properties as a function of temperature,
- Non-linear, thermal boundary conditions, and
- Moving boundaries.

For pyrolyzing ablators, the following additional capabilities must be included:

- Non-linear, time-dependent quasi-solid in-depth reactions,
- Transport and thermal properties as a function of material state as well as temperature,
- Inclusion of the thermal effects of gas flow within the bulk material, and
- In-depth pore pressure due to pyrolysis gas transport (not always employed).

Many commercial finite element codes possess these computational capabilities and have been applied to the analysis of ablation as demonstrated in References 17 through 24. Additionally, most commercial finite element programs possess the capability to solve problems in one, two, or three spatial dimensions, which is required to meet the needs of advanced spacecraft design.

In this work, we demonstrate the capability to model pyrolyzing ablation using the commercial code COMSOL Multiphysics® (COMSOL, Inc., Burlington, Massachusetts). COMSOL Multiphysics® is a general-purpose software platform, based on advanced numerical methods, for modeling and simulating physics-based problems. COMSOL Multiphysics® can solve algebraic, and ordinary partial differential equations in one, two, and three dimensions. The equations can be solved either fully coupled, or by various decoupled schemes. The work here demonstrates that non-pyrolyzing and pyrolyzing ablators can be modeled using COMSOL Multiphysics® in both one and two dimensions, and that the extension to three-dimensional problems is feasible.

II. Physical Phenomena

Figure 1 illustrates the general physical problem being modeled here. A pyrolyzing material composed of multiple decomposing and non-decomposing constituents is heated from the upper surface. As the material is heated from convective or radiative energy, this thermal energy applied at the surface raises the surface temperature. As a result, surface material is removed through either vaporization or mechanical removal. A certain amount of thermal energy is also transferred in-depth by way of conduction, raising the internal temperature and resulting in pyrolysis and decomposition of the material. This decomposition produces gases that travel upward toward the surface, leaving behind a porous residue, which for many materials of interest is a carbonaceous char, possibly reinforced with refractory fibers or cloth. At the material backface, the conducted energy can be transferred out of the material either by convection or radiation into a thermal sink at a specified temperature, or, in many cases, the backface is simply adiabatic.

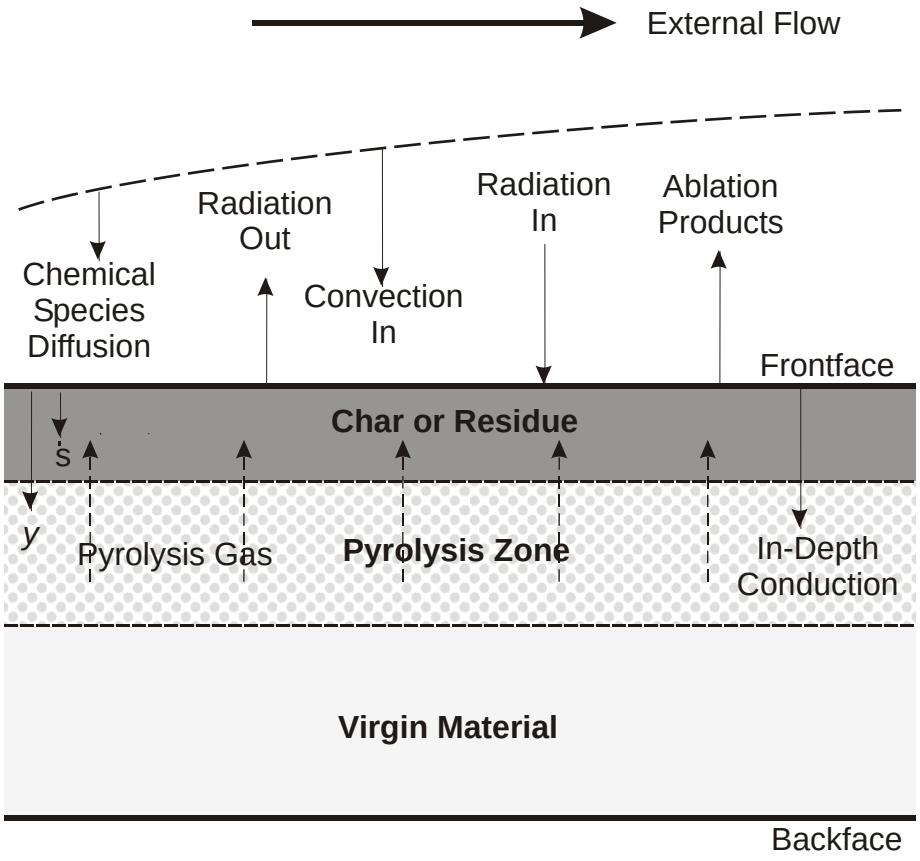

Figure 1. General problem illustration.

III. Material Modeling Methodology

In this section we review the fundamental modeling assumptions and associated mathematical description of pyrolyzing ablators.

A. Material Decomposition Model

Many decomposing pyrolyzing materials appear to behave as three independently pyrolyzing components, therefore, the model presented here uses a three-component decomposition model (although the restriction on the number of components can be relaxed if necessary). The resin filler is presumed to consist of two components which decompose separately; the reinforcing material is the third component, which can also decompose. The instantaneous density of the composite is given by Eq. (1):

$$\rho = \Gamma(\rho_A + \rho_B) + (1 - \Gamma)\rho_C \tag{1}$$

where A and B represent components of the resin, C represents the reinforcing material, and Γ is the volume fraction of resin and is an input quantity.

Each of the three components can decompose following a general relation as proposed by Goldstein[25] and shown as Eq. (2):

$$\left(\frac{\partial \rho_i}{\partial t}\right)_y = -A_i \exp\left(-\frac{E_i}{RT}\right)\rho_{o,i}\left(\frac{\rho_i - \rho_{r,i}}{\rho_{o,i}}\right)^{\psi_i} \tag{2}$$

where $\rho_{r,i}$ is the residual or terminal density of component i, and $\rho_{o,i}$ is the original, virgin material density of component i. The values $\rho_{o,i}$, $\rho_{r,i}$, A_i, E_i and ψ_i are input parameters for $i = A, B, C$ for the main material. Equations (1) and (2) are coupled with an expression that provides a history of the temperature and density to determine the material decomposition rate.

B. Surface Thermochemistry

Material mass loss during ablation occurs by two distinct mechanisms: in-depth pyrolysis and surface mass loss removal. In-depth pyrolysis occurs as the material decomposes as described by the reaction in Eq. (2) above. Surface mass loss removal can occur through vaporization or by removal of the surface in sold or liquid form (discrete removal). We assume here that surface mass loss occurs only by vaporization; however, the capability to account for discrete mass removal could easily be added to the model.

The surface mass loss rate can be determined by assuming surface thermochemical and kinetic relationships, which can be expressed as a function of four variables as shown in Eq. (3):

$$\dot{m}_c = \dot{m}_c(p, \dot{m}_g, \rho_e u_e C_M, T_s) \tag{3}$$

If equilibrium conditions between the solid and the gas can be assumed, however, then the relationship in Eq. (3) can be reduced by one dimension by normalizing the mass loss rates by the mass transfer coefficient $\rho_e u_e C_M$ such that Eq. (4):

$$B_c' = B_c'(p, B_g', T_s) \tag{4}$$

where the normalized char mass loss rate $B_c^{'}$ and pyrolysis mass loss rate $B_g^{'}$ are defined as shown in Eqs. (5) and (6):

$$B_c' = \dot{m}_c / \rho_e u_e C_M \tag{5}$$

$$B_g' = \dot{m}_g / \rho_e u_e C_M \tag{6}$$

and the total normalized mass loss rate B' is the sum of the normalized pyrolysis mass loss rate B_g' and the normalized char mass loss rate B_c' as seen in Eq. (7):

$$B' = B_c' + B_g' \tag{7}$$

Typically, the relationship expressed in Equation (4) is obtained using a set of tables providing the normalized mass loss rate B' as a function of surface pressure, surface temperature, and char gas mass flowrate calculated from a separate program. The tables represent a three-dimensional relationship between the normalized char mass loss B_c' and the pressure p, normalized pyrolysis mass loss rate B_g', and surface temperature T_s.

The surface recession rate $\dot{s}$ is therefore equal to the normalized surface char mass loss rate multiplied by the mass transfer coefficient $\rho_e u_e C_M$ divided by the surface densityρ_s , thus Eq. (8):

$$\dot{s} = \rho_e u_e C_M \cdot B_c' / \rho_s \tag{8}$$

Additionally, the enthalpy of the gas phase just above the surface also follows this three-dimensional relationship such that Eq. (9):

$$h_w = h_w(p, B_g', T_s) \tag{9}$$

C. In-Depth Thermal Transport and Surface Optical Properties

The local specific heat and thermal conductivity are formulated from separate virgin and char material properties, $C_{p,v}$, $C_{p,c}$, k_v, and k_c. In partially-pyrolyzed zones ($\rho_c < \rho < \rho_v$), the specific heat is formulated with a special mixing rule, as shown in Eqs. (10) and (11):

$$k = xk_v + (1-x)k_c \tag{10}$$

$$C_p = xC_{p,v} + (1-x)C_{p,c} \tag{11}$$

where the weighting variable x is based on the convenient function that partially-pyrolyzed material is a simple mixture of pure virgin material and pure char. Other mixing rules are possible and sometimes used. The quantity x is defined as the mass fraction of pure virgin material in this imaginary mixture, which yields the correct local density, as shown in Eq. (12):

$$x = \frac{\rho_v}{\rho_v - \rho_c}\left(1 - \frac{\rho_c}{\rho}\right) \tag{12}$$

The emissivity and absorptivity of the material in any state of decomposition are calculated similarly to the method used for specific heat and thermal conductivity. That is, Eqs. (13) and (14):

$$\varepsilon = x\varepsilon_v + (1-x)\varepsilon_c \tag{13}$$

$$\alpha = x\alpha_v + (1-x)\alpha_c \tag{14}$$

The virgin and char solid enthalpies are calculated based on the thermodynamic definition given as Eq. (15):

$$h = \int_{T_0}^{T} C_p dT + h_0 \tag{15}$$

where h_0 is the enthalpy of formation at the reference temperature T_0 (taken to be 298.15 K). The enthalpy for a partially-pyrolyzed material, Eq. (16), uses the same mixing rule for specific heat and thermal conductivity as seen in Eqs. (10) and (11):

$$h = xh_v + (1-x)h_c \tag{16}$$

D. Energy Equation

The solution for the time evolution of the decomposing composite requires the local temperature as a function of time. One possibility is to specify the temperature as an explicit function of time or compute the temperature at each location within the composite using the energy equation that takes the form of a partial differential equation in space and time.

The applicable energy equation for a pyrolyzing material in a coordinate system fixed in space is Eq. (17):

$$\rho C_p\left(\frac{\partial T}{\partial t}\right) = \frac{1}{A}\nabla(kA\nabla T) + \frac{1}{A}\nabla\cdot\left(\dot{\boldsymbol{m}}_{\boldsymbol{g}} h_g A\right) - \bar{h}(T)\left(\frac{\partial \rho}{\partial t}\right) \tag{17}$$

in which the terms in order from left to right represent: 1) internal energy storage, 2) energy transport by thermal conduction, 3) energy transport by pyrolysis gas convection, and 4) chemical energy release due to pyrolysis.

The quantity $\bar{h}$ is computed from temperature-dependent virgin and char enthalpies ($h_v(T)$ and $h_c(T)$, respectively) and is an input to the model computed from the virgin and char densities and the virgin and char enthalpies, as seen in Eq. (18):

$$\bar{h}(T) = \frac{\rho_v h_v(T) - \rho_c h_c(T)}{\rho_v - \rho_c} \tag{18}$$

Because of surface ablation, the surface recedes at a rate given by Eq. (19):

$$\dot{s} = \frac{\dot{m}_c}{\rho_s} = \rho_e u_e C_M B_c' / \rho_s \tag{19}$$

For a one-dimensional planar material, the energy equation can be simplified and written in a coordinate system y fixed to the ablating surface, as shown in Eq. (20):

$$\rho C_p \left(\frac{\partial T}{\partial t}\right)_y = \frac{1}{A}\frac{\partial}{\partial y}\left(kA\frac{\partial T}{\partial y}\right)_t - \bar{h}(T)\left(\frac{\partial \rho}{\partial t}\right)_y + \dot{s}\rho C_p \left(\frac{\partial T}{\partial y}\right)_t + \frac{1}{A}\left(\frac{\partial \dot{m}_g h_g A}{\partial y}\right)_t \tag{20}$$

At long times and for thick samples, the recession rate of an ablating material can reach a steady state in which energy flow due to conduction is balanced by convection of the solid material and the pyrolysis gases.

For a one-dimensional planar geometry in a coordinate fixed to moving surface, the energy equation can be transformed into the form shown in Eq. (21):

$$\frac{\partial}{\partial y}\left(k\frac{\partial T}{\partial y}\right) + \left(\frac{\partial \dot{m}_g h_g}{\partial y}\right) + \dot{s}\left(\frac{\partial \rho h_s}{\partial y}\right) = 0 \tag{21}$$

which eliminates the term containing the time derivative. In the y coordinate space, the temperature profile appears unchanged with time even though the surface is receding and the temperature profile moves through the material.

When steady-state conditions occur, it is possible to write the energy balance around a control volume extending just above the ablating surface and far down into the material where the temperature has reached ambient material conditions, as shown in Fig. 2.

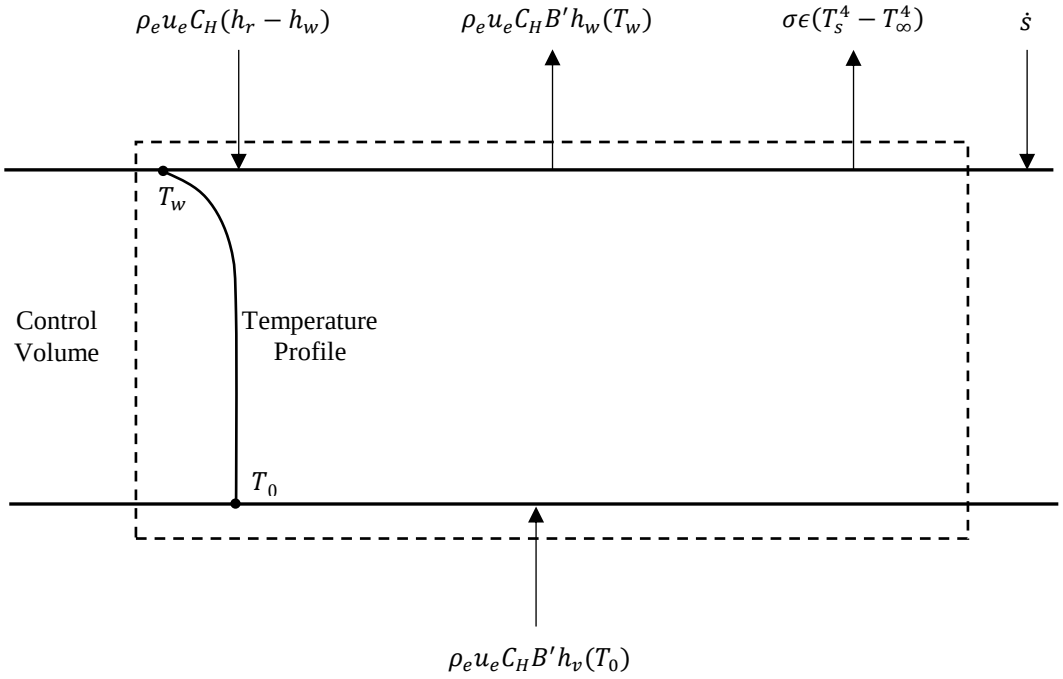

Figure 2. Energy balance and control volume for steady-state ablation.

An energy balance around the control volume shown in Fig. 2 results in Eq. (22):

$$\rho_e u_e C_H (h_r - h_w) - \rho_e u_e C_H B' (h_w - h_v) - \sigma\epsilon(T^4 - T_\infty^4) = 0 \tag{22}$$

where the terms in Eq. (22) represent in order from left to right: convective flux, energy due to mass removal, and reradiation. Note that the energy balance is independent of the specific heat transfer and decomposition processes occurring within the material. The total mass loss rate is composed of the in-depth pyrolysis mass flux $\dot{m}_g$ and the surface char flux $\dot{m}_c$, but only the total mass flux needs to be determined and knowledge of the values of the individual fluxes is not needed in the energy balance.

Solution for the steady-state temperature and mass loss is obtained by solving the overall energy balance in Eq. (22) in conjunction with the surface thermochemical relationships, Eq. (23):

$$B_c' = B_c'(p, B_g', T_s) \text{ and } h_w = h_w(p, B_g', T_s) \tag{23}$$

where again, Eq. (24):

$$\dot{s} = \frac{\dot{m}_c}{\rho_s} = \frac{\rho_e u_e C_M B_c'}{\rho_s} \tag{24}$$

Finally, since steady-state conditions occur, the ratio of the char to pyrolysis mass flux and can be expressed as Eq. (25):

$$\frac{B_c'}{B_g'} = B_{ss} \tag{25}$$

where B_{ss} is a constant based on the decomposition characteristics of the constituent components of the composite and is computed from the virgin and char densities.

E. Surface and Backface Boundary Conditions

At the moving ablating material surface, the boundary conditions require the specification of the surface temperature and the recession. These can be specified explicitly or can determined from a surface energy balance and equilibrium or non-equilibrium thermodynamic relationships applied between the ablating surface material and gas phase.

The simplest boundary condition specifies the surface recession rate and temperature. This condition is expressed as Eq. (26):

$$T_w = T_s \tag{26}$$

and Eq. (27):

$$\dot{s} = \dot{s_s} \tag{27}$$

When the heat fluxes to the surface, but not the surface temperature and recession rate, are known, a general surface energy balance with recession can be used to determine the surface temperature and can be expressed as shown in Eq. (28):

$$\alpha I + \rho_e u_e C_H (h_r - h_w) + k\frac{\partial T}{\partial y} - F\sigma\varepsilon(T_w^4 - T_\infty^4) - \rho_e u_e C_H \left(B' h_w - B_c' h_c - B_g' h_g\right) = 0 \tag{28}$$

where heat input from radiation and convection is balanced by heat loss from conduction, surface reradiation, and surface material ablation. Equation (28) assumes that the heat and mass transfer coefficients are equal, that is, $C_H = C_M$.

The convective heat and mass transfer coefficients are reduced by blowing from the surface and corrected using an expression derived from film theory[26] as shown in Eq. (29):

$$\frac{C_H}{C_{Ho}} = \frac{C_M}{C_{Mo}} = \frac{\ln(1 + 2\lambda B')}{2\lambda B'} \tag{29}$$

where C_H and C_M are the corrected or "blown" transfer coefficients and C_{Ho} and C_{Mo} are the unblown values. For these analyses, equal heat and mass transfer coefficients were assumed so that $C_M = C_H$. Equations (29) and (23) provide two independent relationships and, in conjunction with Eq. (24), allow the surface temperature and recession rate to be determined. The assumption of equal heat and mass transfer coefficients is valid if the Lewis number is close to unity, which is approximately true for many gases.

At the material backface where no ablation is assumed to occur, the general boundary condition is as shown by Eq. (30):

$$k\frac{\partial T}{\partial y} - h(T_b - T_\infty) - F\sigma\varepsilon\left(T_b^4 - T_\infty^4\right) = 0 \tag{30}$$

where in-depth energy conduction from the material surface feeds convective and radiative heat losses into the backface environment. The backface "sink" temperature T_∞ and heat transfer coefficient h can be functions of time while the emissivity ε and material thermal conductivity k are functions of material and temperature. Often, however, adiabatic conditions are also assumed.

IV. Examples

The following sections present five examples of common ablation problems solved with the COMSOL program. All of the examples use the Theoretical Ablative Composite for Open Testing (TACOT) material model as described in the appendix. These examples are a set of high-level tests, but many more low-level functionality tests were performed.

A. Example 1: Thermogravimetric Analysis (TGA)

In a thermogravimetric analysis (TGA), a sample of the material is heated at a specified rate. The sample mass loss as a function of temperature is recorded and the derivative of mass loss with respect to temperature is used to determine the constants in Eq. (2). The heating rate can vary, but is usually in the range of 10-50 K/s. The temperature versus time history can therefore be represented by the expression in Eq. (31):

$$T = \beta t + T_0 \tag{31}$$

where T is the instantaneous material temperature, T_0 is the initial temperature, and β is the heating rate.

Differentiating Eq. (1) provides the governing equation to be solved in conjunction with the individual density rate changes given by Eq. (2) and the temperature provided by Eq. (32).

$$\frac{d\rho}{dt} = \Gamma\left(\frac{d\rho_A}{dt} + \frac{d\rho_A}{dt}\right) + (1 - \Gamma)\frac{d\rho_C}{dt} \tag{32}$$

Determination of the composite density therefore involves the time-integration of Eq. (32) incorporating the three independent density decomposition rates $d\rho_A/dt, d\rho_B/dt,$ and ρ_C/dt.

Predicted sample density versus temperature is shown in Fig. 3. Two solutions of the integration of Eq. 32 are shown, one using the COMSOL code and a second, separate calculation using an explicit, fourth-order Runge-Kutta

integration scheme. The relative difference between the two calculations is also shown. Overall, the two calculations agree extremely well, with the difference being less 0.14% over the entire density range.

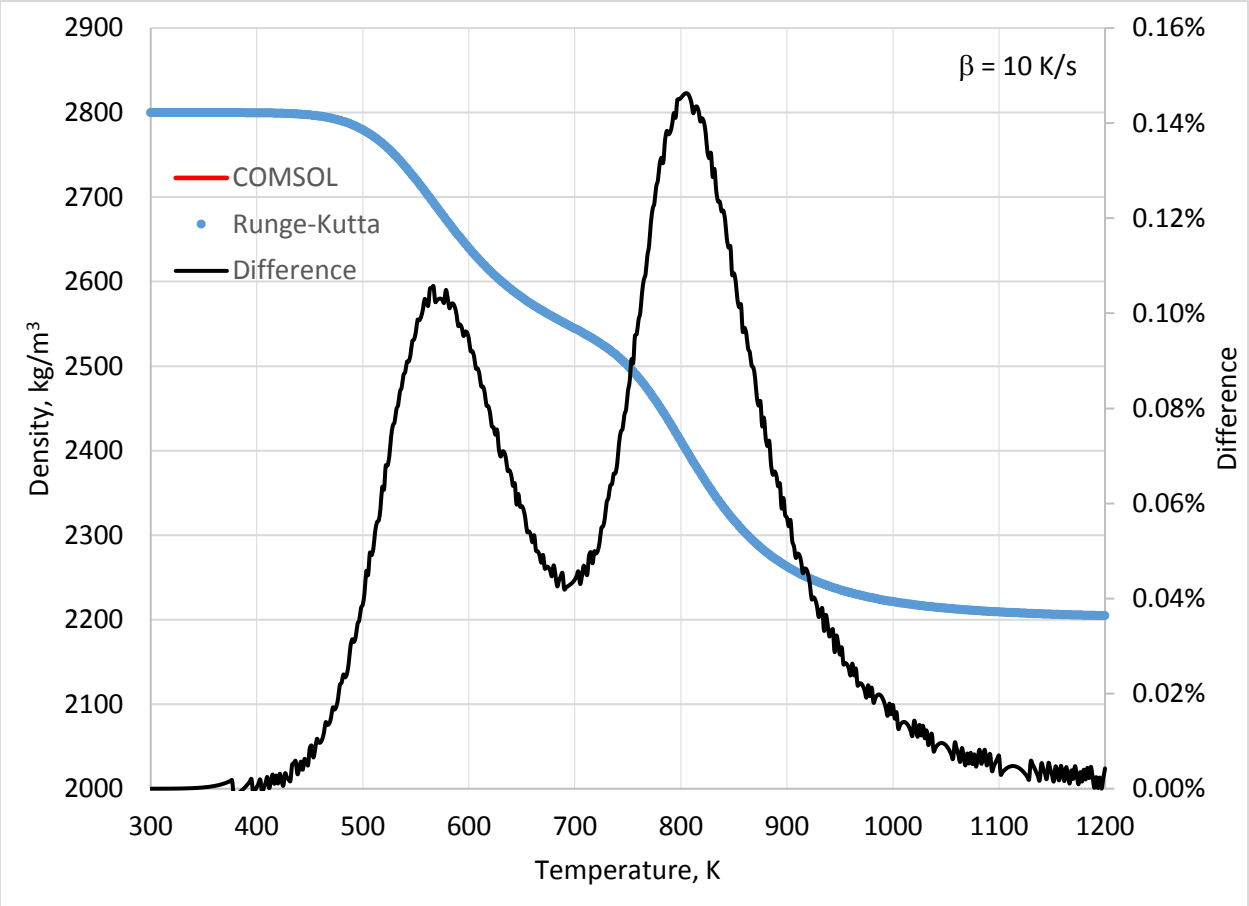

Figure 3. Comparison of predicted density using COMSOL and the Runge-Kutta explicit model. The difference between the two solutions is also shown.

A similar plot for the absolute value of the decomposition rate is shown in Fig. 4. The difference between the two models for the decomposition rate is less than 0.01%.

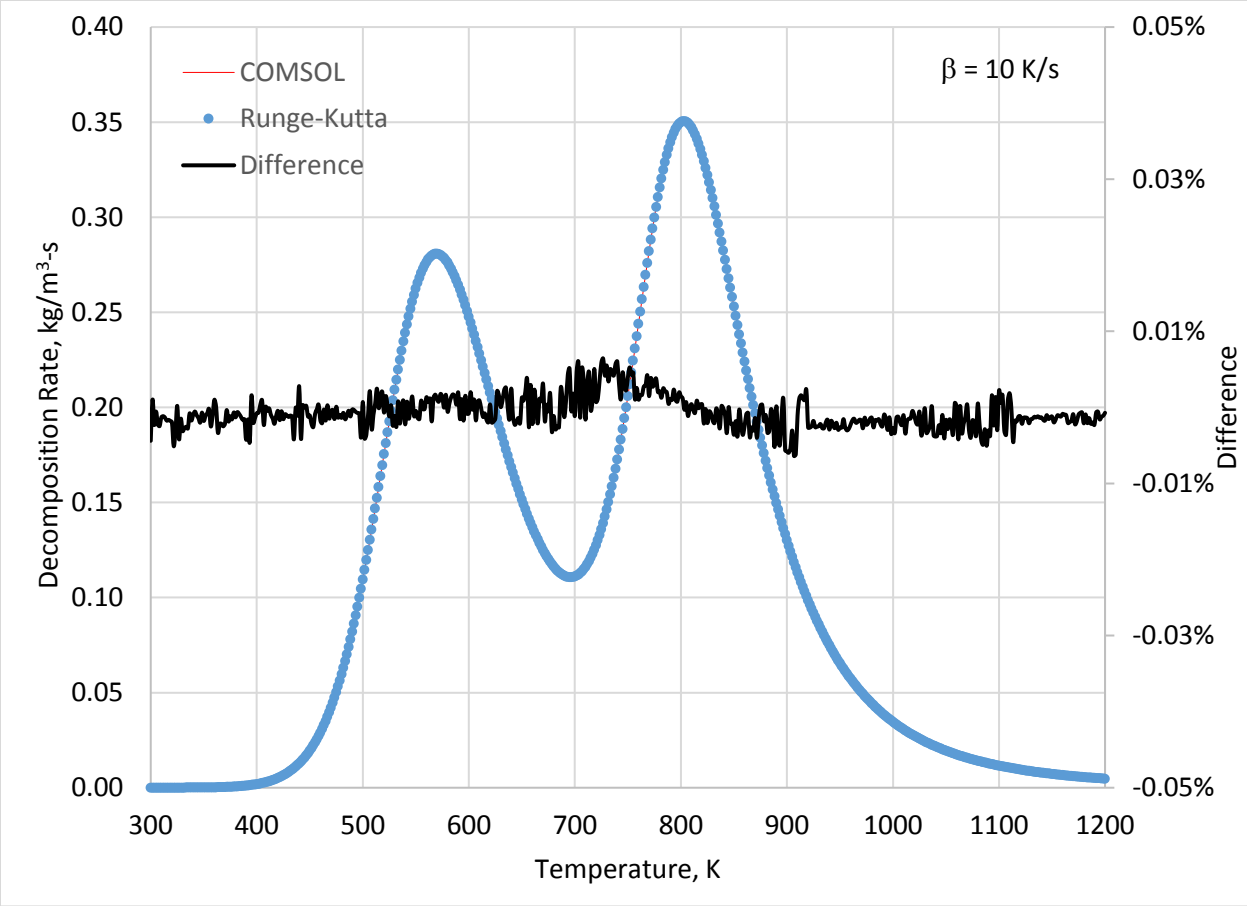

Figure 4. Comparison of predicted density decomposition rate (absolute value) using COMSOL and the Runge-Kutta explicit model. The difference between the two solutions is also shown.

B. Example 2: Steady-state Ablation Analysis

Computing the steady-state ablation rate of the pyrolyzing composite subjected to surface heating resulting in a temperature gradient from the surface requires the solution of Eq. (22), which is a non-linear algebraic equation (not a differential equation): Additionally, the expressions in Eq. (23) are also included in the solution process. Equation (23) usually takes the form a table of values providing the normalized char mass loss rate and gas phase enthalpy as a function of surface temperature, normalized pyrolysis mass loss rate, and pressure calculated from a thermochemical equilibrium code. Alternatively, these relationships can be incorporated directly as an explicit calculation.

At steady state, the ratio of char to pyrolysis mass loss is a fixed value given by the composition of the base material. The appendix shows that the for the TACOT material the ratio of char to pyrolysis mass loss is 3.666, so that the final constraint becomes as shown in Eq. (33):

$$\frac{B_c'}{B_g'} = 3.666 \tag{33}$$

For this example, the free-stream recovery enthalpy and surface heat transfer rates were specified, but varied across a nominal range of values (freestream enthalpy from 10 to 100 MJ/kg and mass transfer coefficient from 0.1 to 1.0 kg/m^3-s). Equal heat and mass transfer coefficients were assumed, along with a pressure of 1 atm. Frontface reradiation to an ambient temperature was employed ($T_\infty = 300\ K$).The results for predicted surface temperature using COMSOL are shown in Fig. 5 and are compared to calculations performed using a validated steady-state energy balance computer program (denoted SSEB) developed independently and specifically to solve this problem. Similarly, the results for

normalized mass loss rates are shown in Fig. 6. Excellent agreement between the two calculations is achieved because, on average, the variation between the two solutions is less than 0.1%.

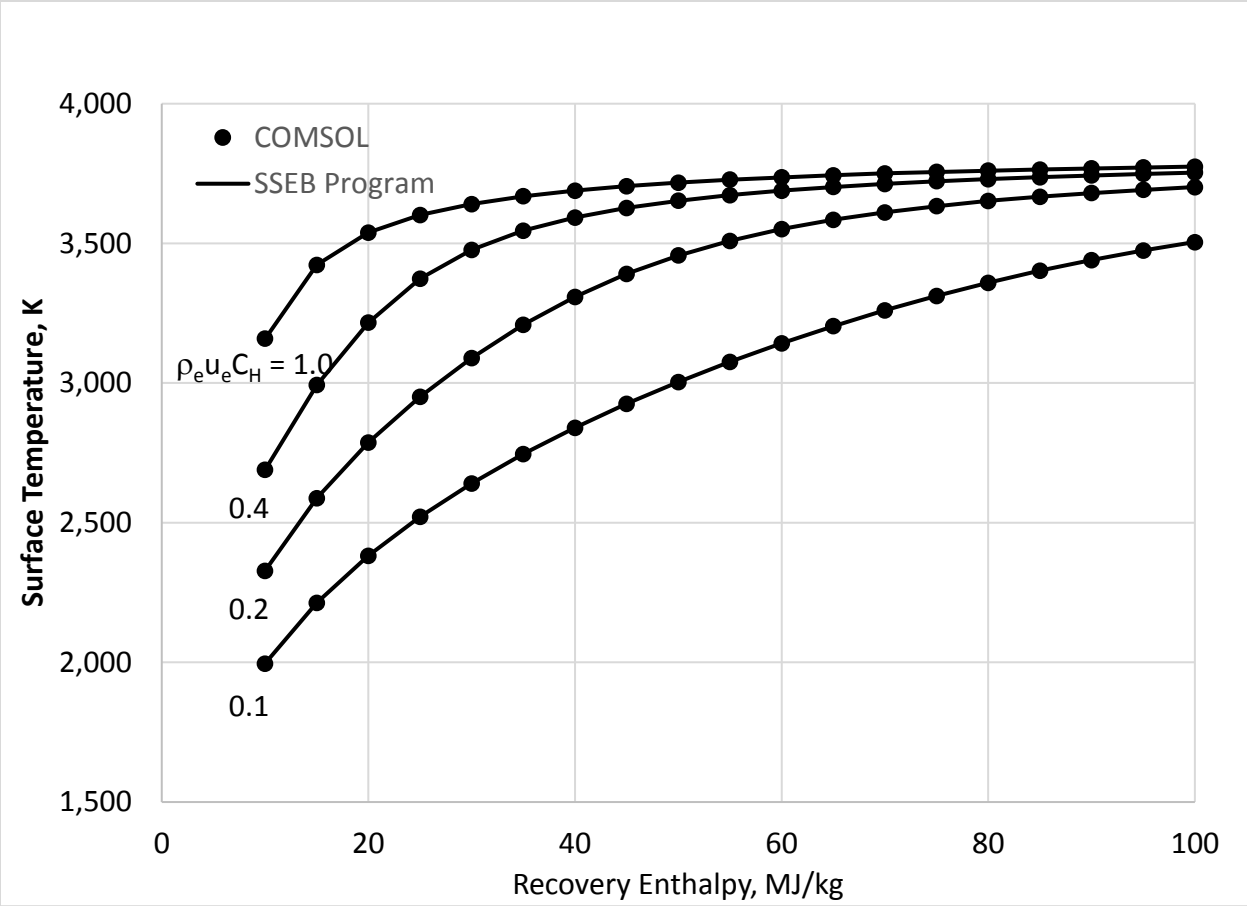

Figure 5. Predicted steady-state surface temperatures as a function of recovery enthalpy for various heat transfer coefficients from the COMSOL program compared to calculated values from a stand-alone program.

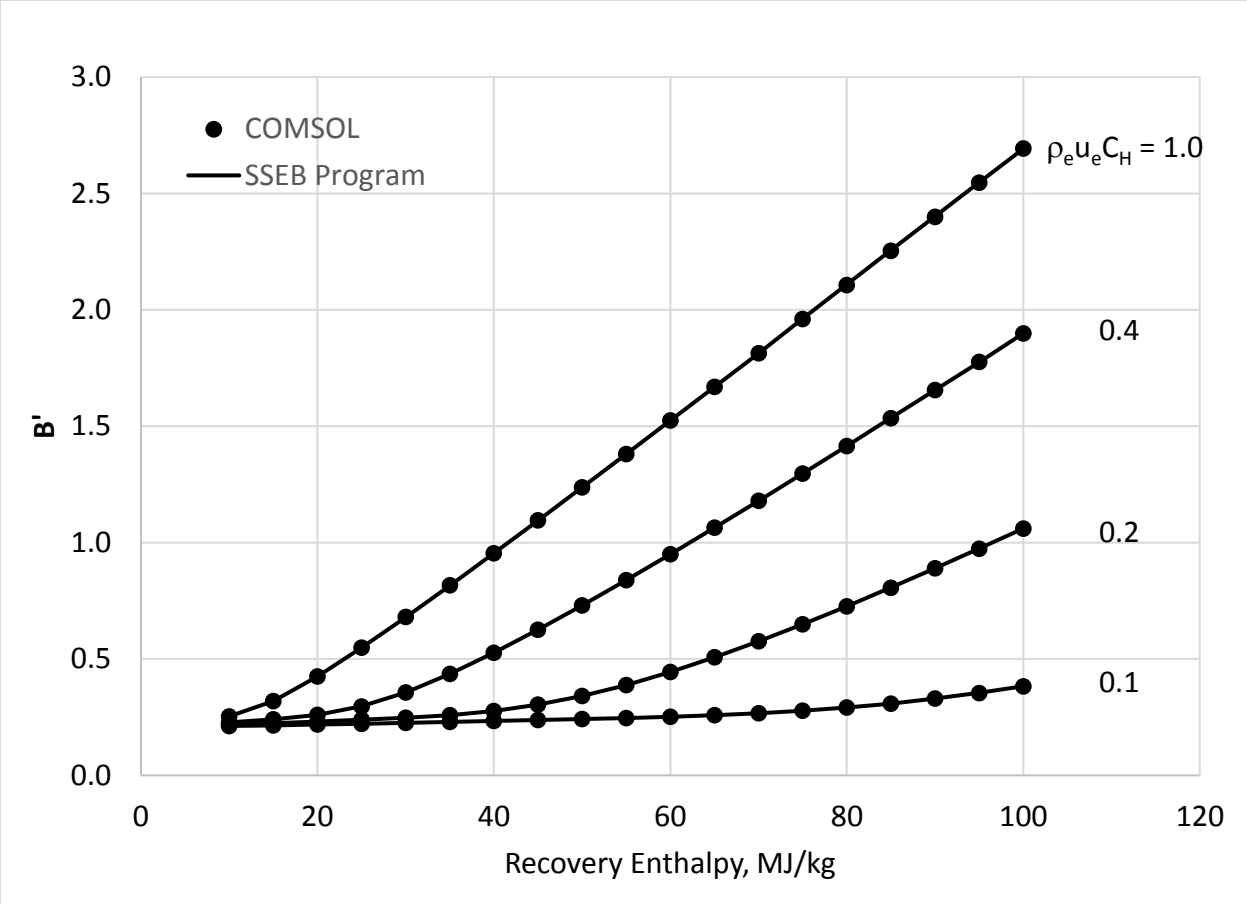

Figure 6. Predicted steady-state normalized mass loss rate as a function of recovery enthalpy for various heat transfer coefficients from the COMSOL program compared to calculated values from a stand-alone program.

C. Example 3: Steady-state In-depth Temperature and Density Profile

While the methodology described in example 2 allows one to calculate the steady-state mass loss rate and surface temperature, it does not allow the determination of the in-depth temperature and density profiles. For a one-dimensional geometry, the transformed energy equation in Eq. (21) is used, and the total pyrolysis mass loss rate at any location y is given by the integral of the local decomposition rate shown in Eq. (34):

$$\dot{m}_g = \int_0^y \left(\frac{\partial \rho}{\partial t}\right)_y dy \tag{34}$$

where the decomposition rate of the composite constituents are given in Eq. (2).

As an example, the steady-state solutions for a planar TACOT geometry with a 3000-K surface temperature and a recession rate of 0.1 mm/s were simulated (Eqs. 21, 26, 27 and 34). A comparison of the results of the steady-state predictions for the TACOT in-depth temperature and density are shown in Fig. 7 and Fig. 8. Two solutions are shown: the COMSOL solution and a separate, independently-developed steady-state, second-order finite difference solution. Both solutions use 161 node points. The agreement between the two solutions is excellent, as is demonstrated by Fig. 7, which shows that the differences between the two temperature solutions is less than 0.25%. Similar agreement is shown in Fig. 8 for the density profile. The maximum difference occurs in the pyrolysis zone at the steep density change, but the difference is less than 0.12%.

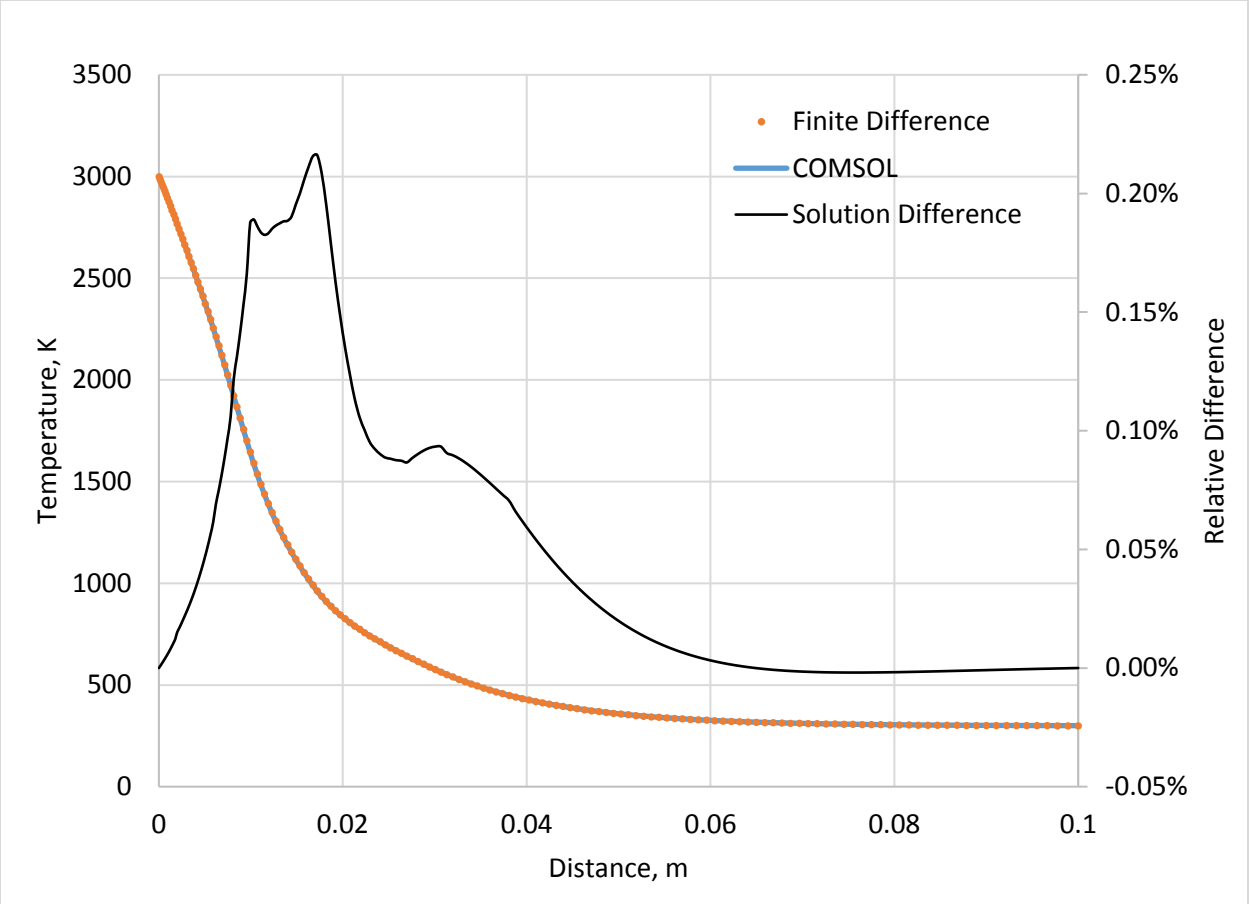

Figure 7. Predicted steady-state temperature profile using COMSOL and a finite difference solution.

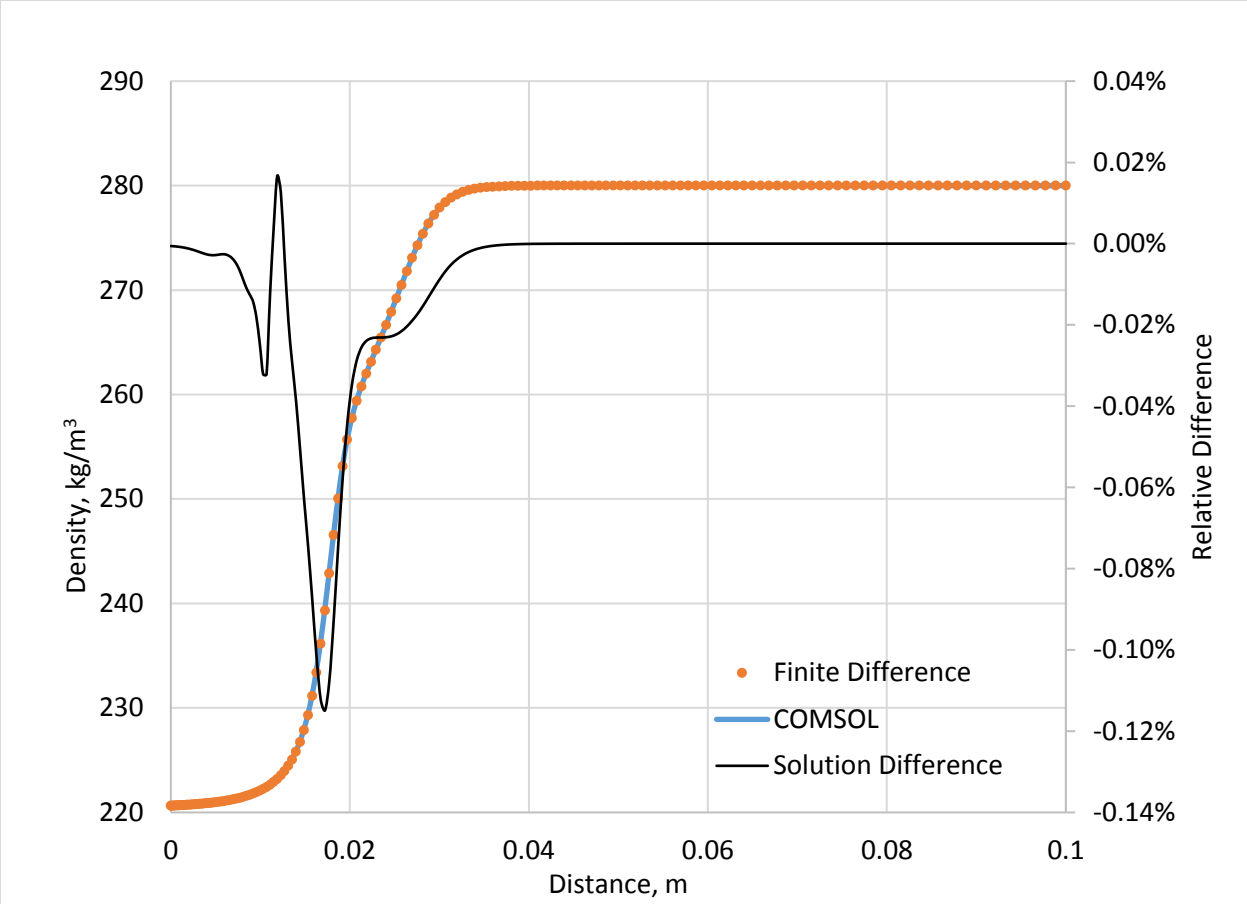

Figure 8. Predicted steady-state density profile using COMSOL and a finite difference solution.

Comparison of the results from COMSOL and FIAT, a well-validated, one-dimensional finite-volume ablation code developed by the NASA Ames Research Center (Moffett Field, California), were also made. The FIAT results are shown in Fig. 10 along with the COMSOL results for the calculated temperature and density. Because FIAT only solves a transient problem, and not the steady-state problem directly, the steady-state solution was determined by solving a very thick slab for a sufficient time until the steady-state condition was reached. In this case, the FIAT solution used was at 2000 s. Examination of the ratio of surface conducted to convected heat flux indicates that at 2000 s the transient simulation has reached within 0.002% of the steady solution.

Figure 9 shows relatively good agreement between the predicted temperatures, but the density in Figure 10 shows more divergence. It is not surprising that the disagreement in density is more pronounced than the temperature, since the density decomposition rate contains terms that are exponential in temperature. Small differences in temperature are therefore magnified in the density results.

The difference between the COMSOL and FIAT solutions does not appear to be due to time step or mesh size, because solutions with finer time steps and mesh sizes did not resolve the difference. Note, however, that much better agreement was obtained between COMSOL and the finite-difference solution presented previously, where the equations and solution methodology in the finite difference solution were known for certain. Although the equations solved by COMSOL and FIAT are supposed to be the same, it is not possible to validate the FIAT solution method further because the actual inner workings and solution algorithm of FIAT are not available.

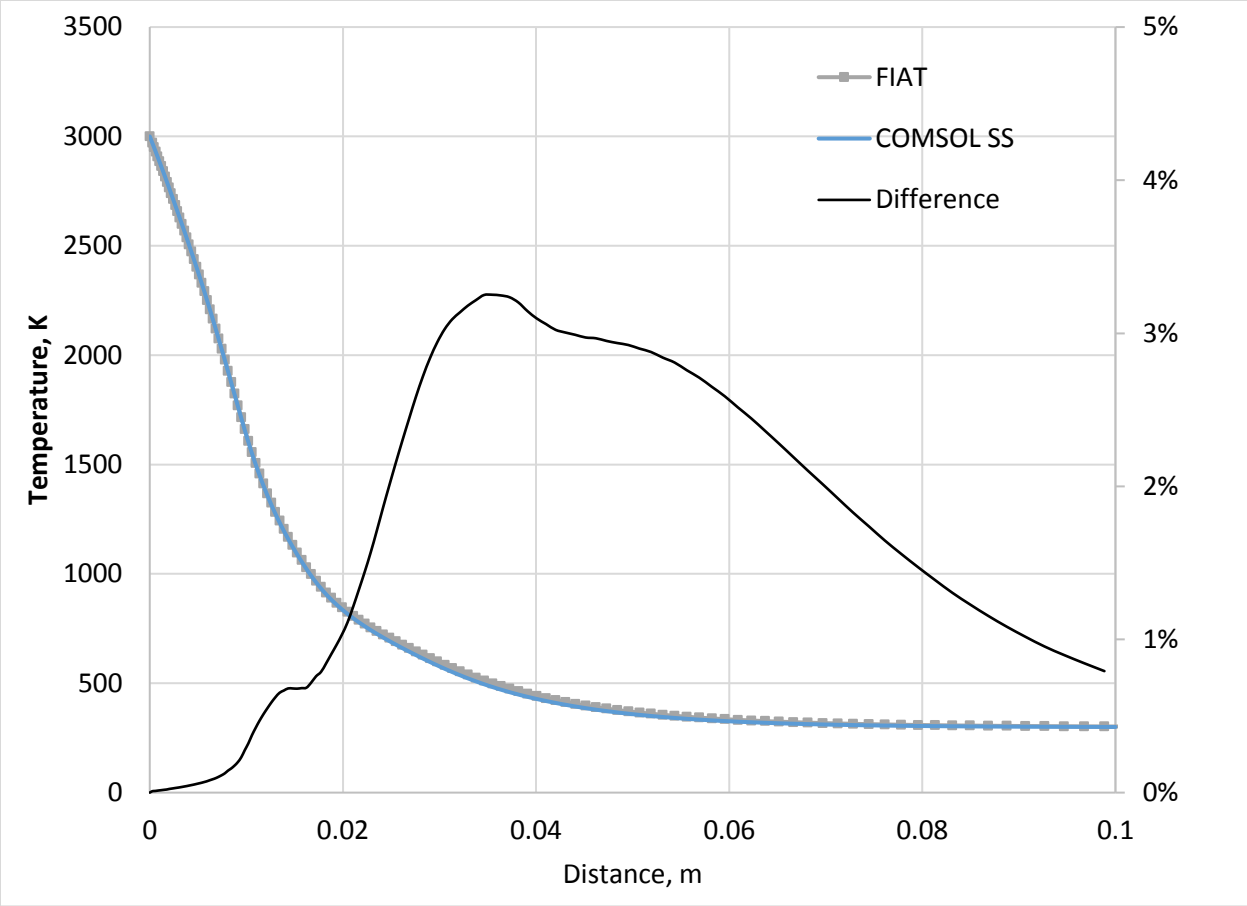

Figure 9. Comparison of steady-state temperature profile between FIAT and COMSOL.

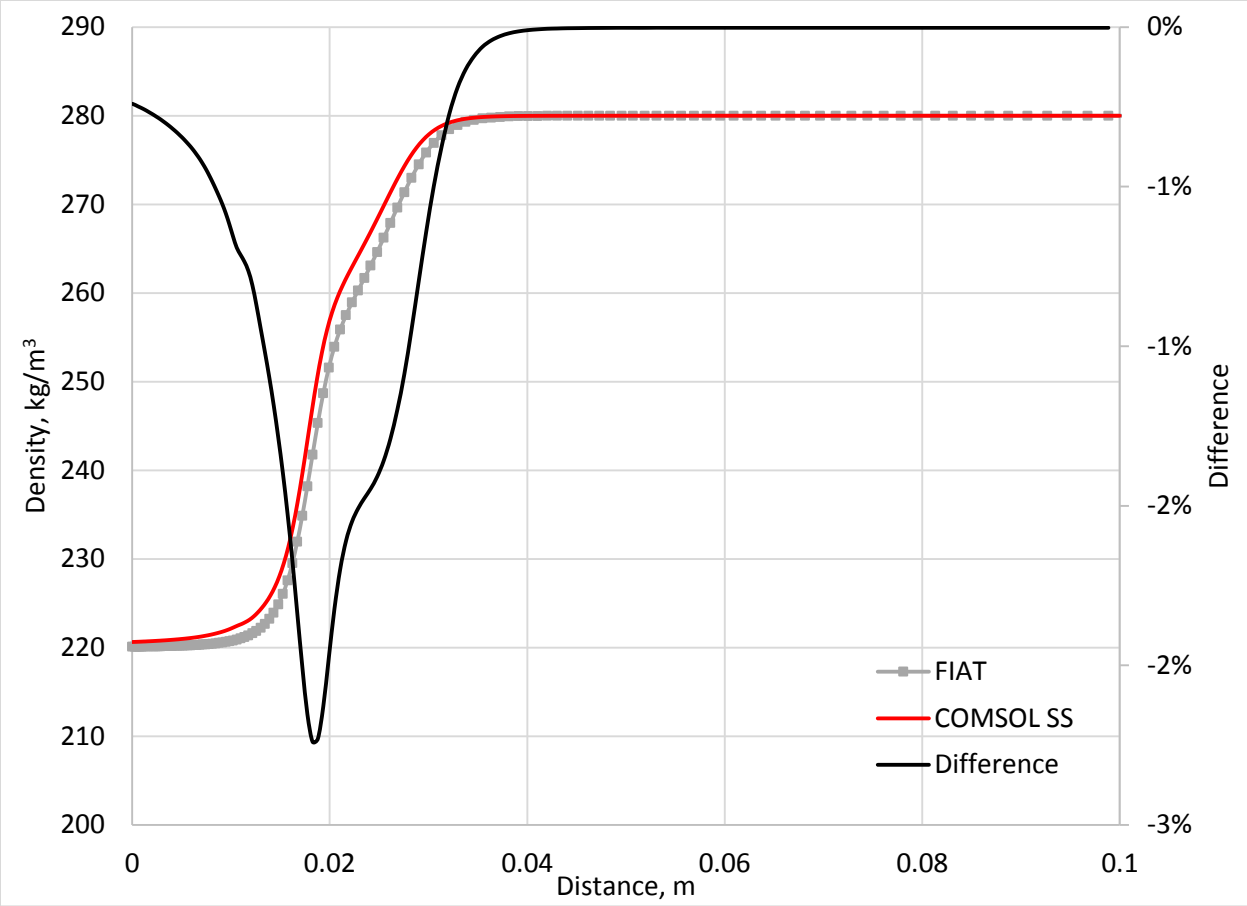

Figure 10. Comparison of steady-state density profiles between FIAT and COMSOL.

D. Example 4: One-Dimensional Transient Analysis for Planar Geometry

The energy equation for a one-dimensional transient analysis assuming a planar geometry is a simplified form of Eq. (20) where the coordinate y is relative to the moving front surface. Equation (20) is solved using the surface thermochemical relationships in Eq. (23), the in-depth decomposition reactions expressed in Eqs. (1) and (2), and the surface energy balance in Eq. (29). The frontface condition used here includes a recovery enthalpy of 40 MJ/kg, a heat transfer coefficient of 0.1 kg/m^2-s, a frontface radiating to ambient conditions, and an adiabatic backface. The sample thickness was 0.05 m and an exposure time of 60 s was calculated. In-depth temperatures were predicted for depths of 0.001, 0.002, 0.004, 0.008, 0.016, 0.024, and 0.05 m from the initial material surface.

Figure 11 compares the predicted frontface surface temperature computed by COMSOL and FIAT. The two solutions agree within 1% even at early times where the relative error is expected to be the greatest. At longer times, the difference drops to approximately 0.1%. Note that the times plotted are not indicative of the solution time steps, which are much smaller.

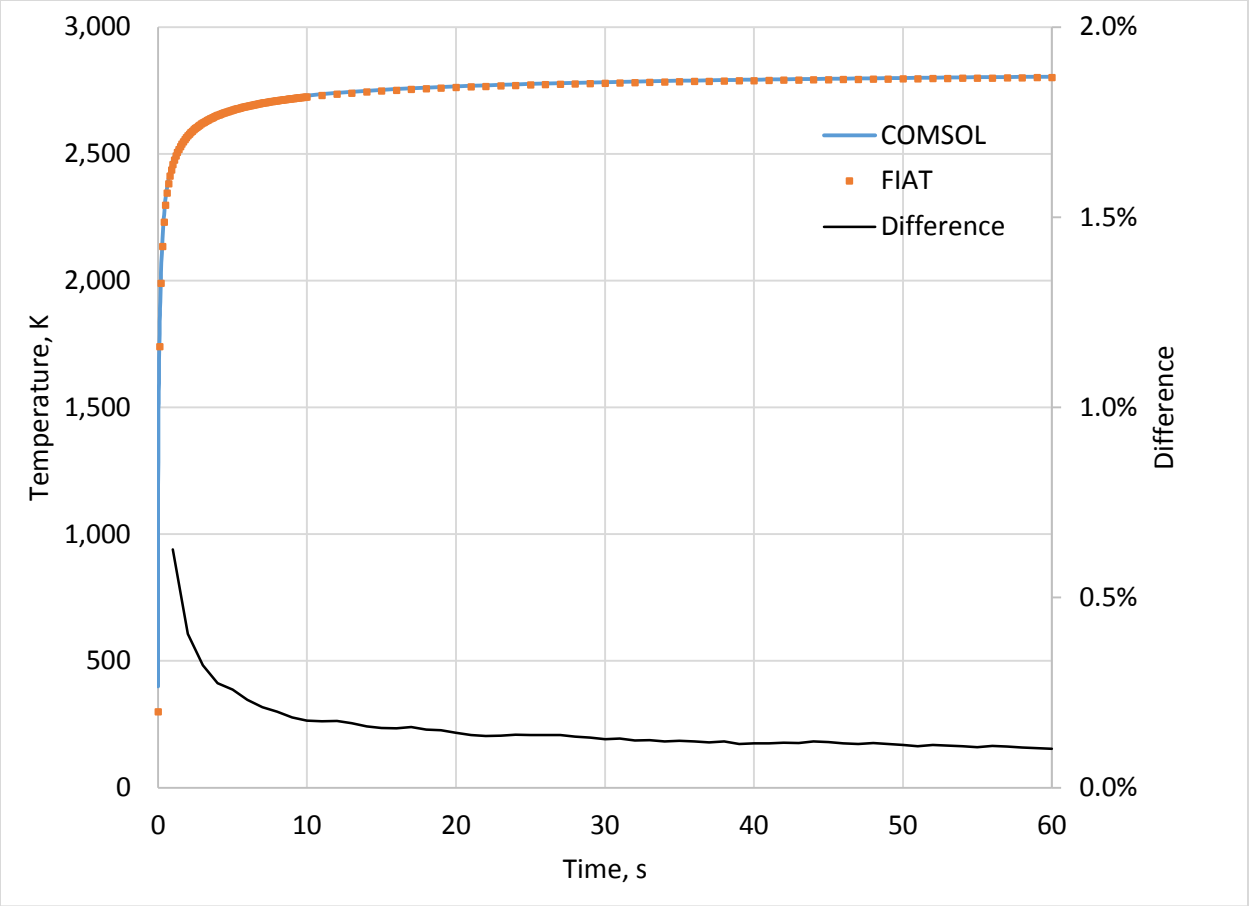

Figure 11. Predicted surface temperature versus time comparing COMSOL and FIAT solutions.

Figure 12 illustrates the computed surface recession from COMSOL and FIAT. Again, the relative difference is approximately 0.1% at long times.

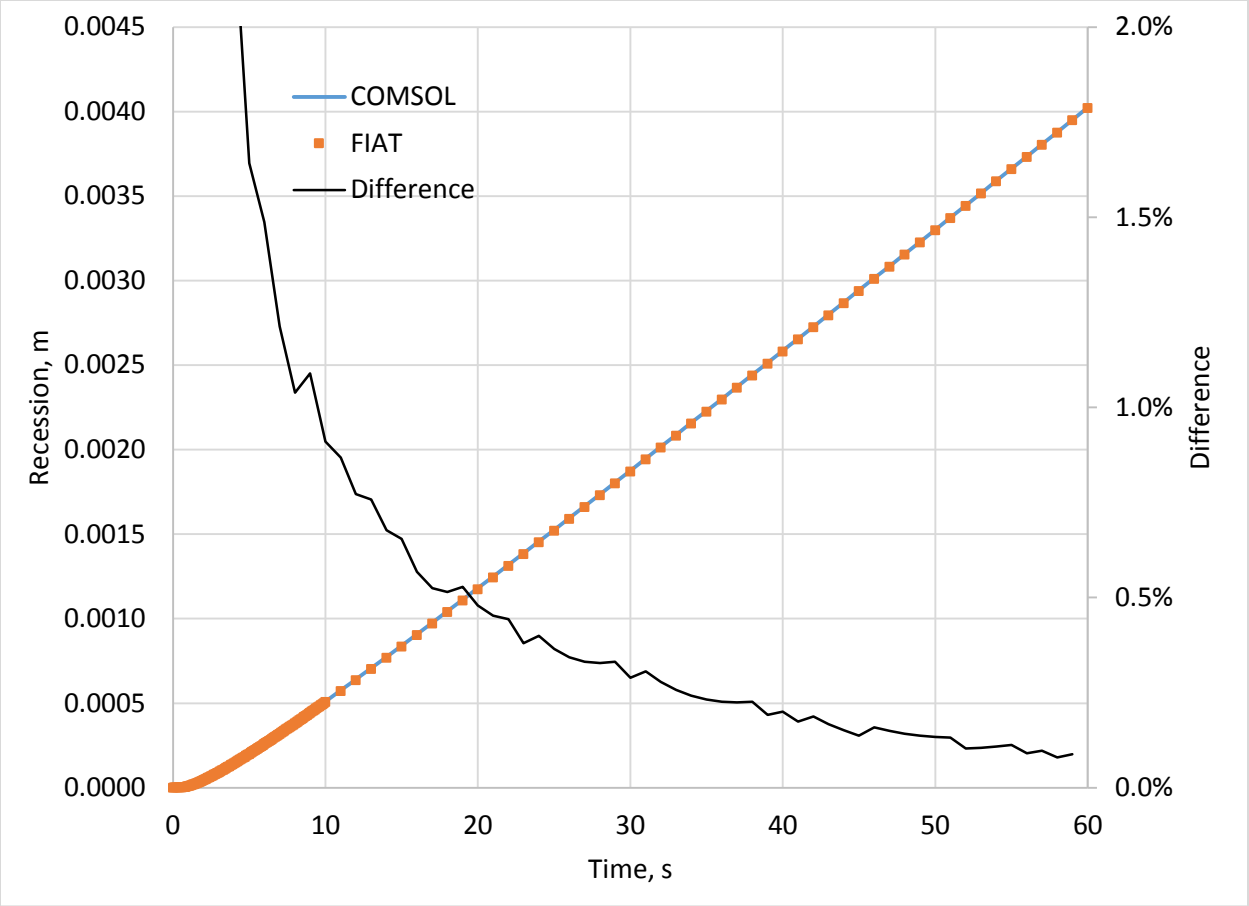

Figure 12. Computed surface recession versus time comparing COMSOL and FIAT solutions.

Figure 13 illustrates the predicted difference between COMSOL and FIAT for the in-depth pyrolysis and surface mass loss rates. The difference here is higher than for surface temperature and recession, but is still remarkably good, agreeing within approximately 3% for the pyrolysis mass loss rate and approximately 1% for the char mass loss rate.

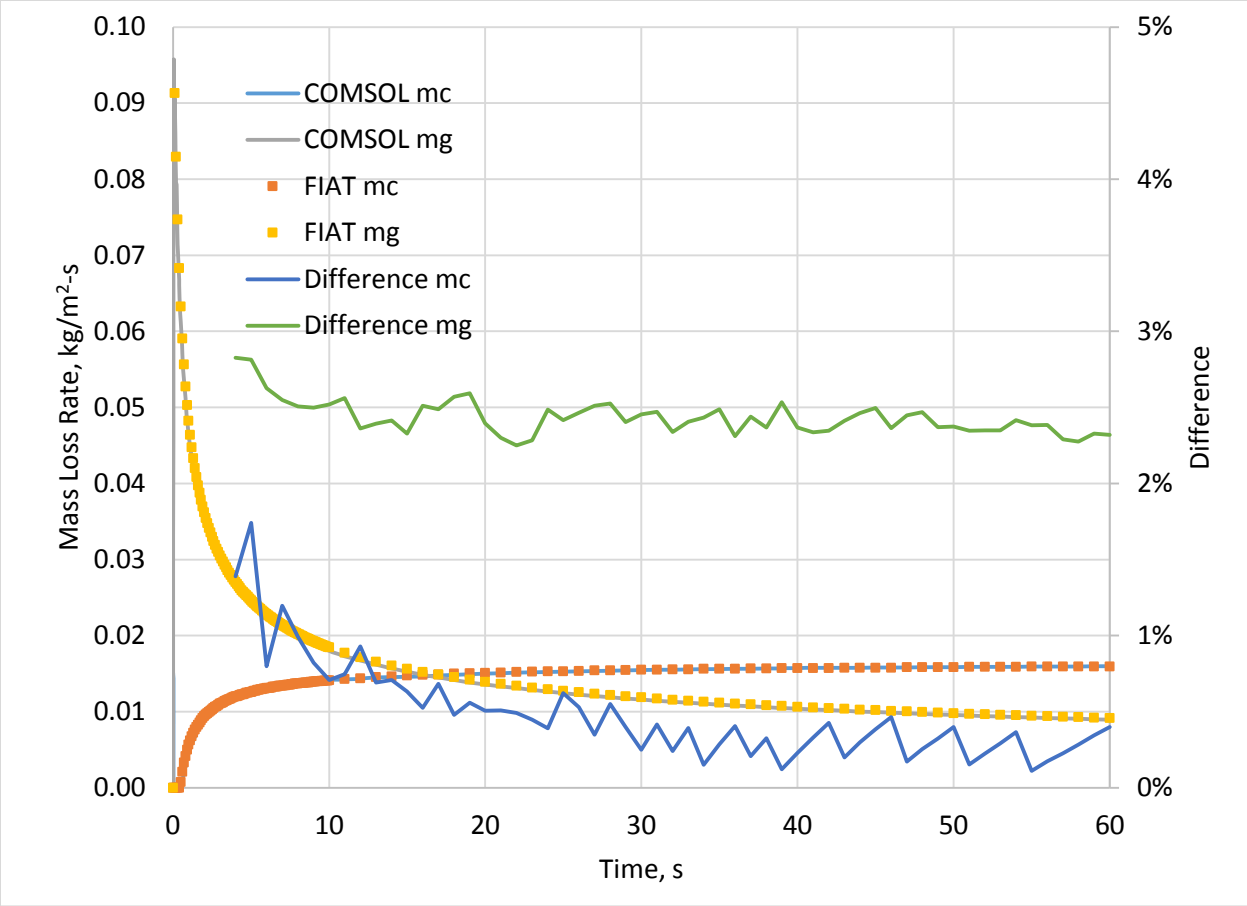

Figure 13. Predicted normalized surface pyrolysis and char mass loss rate versus time comparing COMSOL and FIAT solutions.

Figure 14 illustrates the predicted surface and in-depth temperature histories for the seven selected locations. The agreement is excellent, but there are some differences in the in-depth predictions at later times.

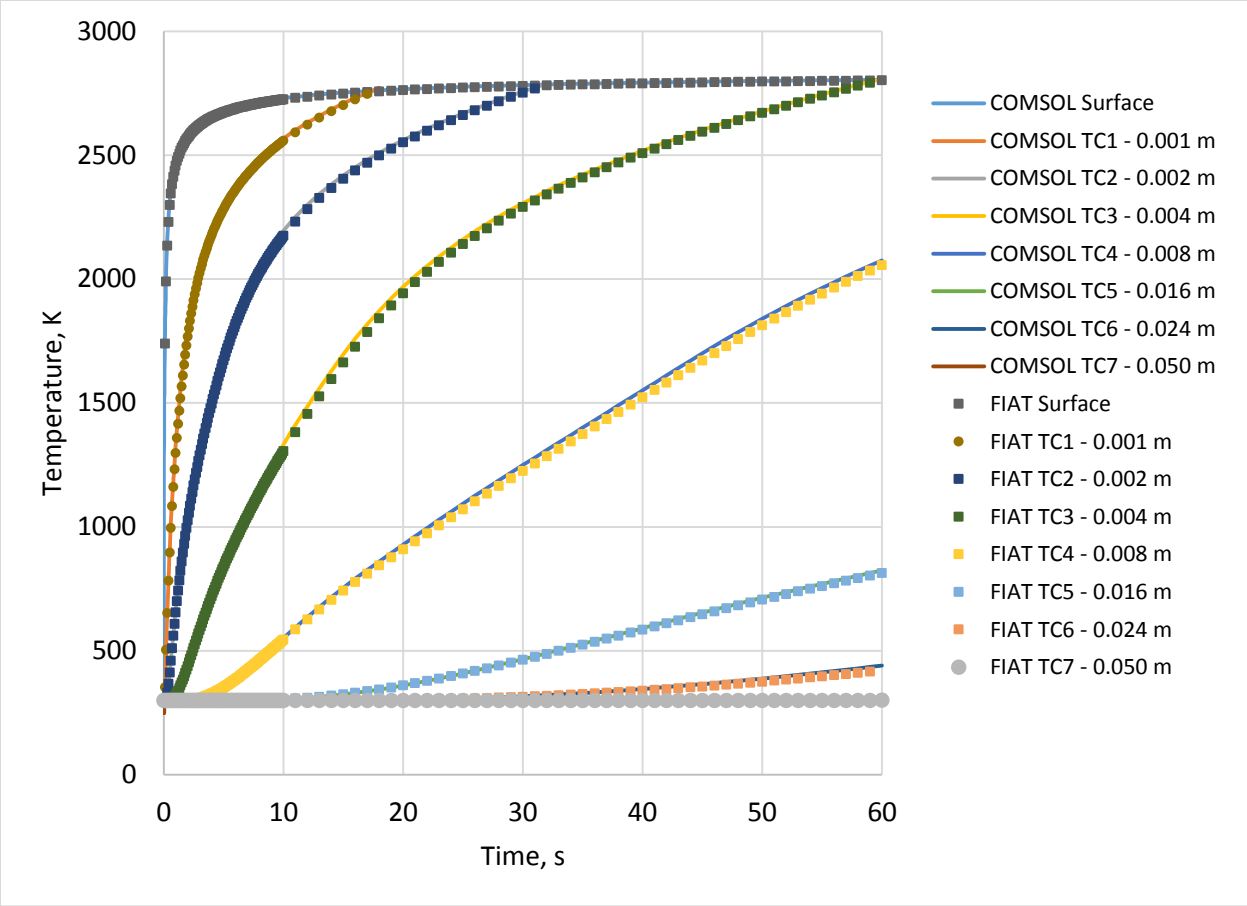

Figure 14. Predicted in-depth temperatures versus time comparing COMSOL and FIAT solutions.

Finally, the predicted temperature and density profiles after the 60-s exposure are plotted in Fig. 15 and Fig 16, respectively. While there is some variation between the profiles, especially the density closer to the surface, the agreement is nonetheless very good.

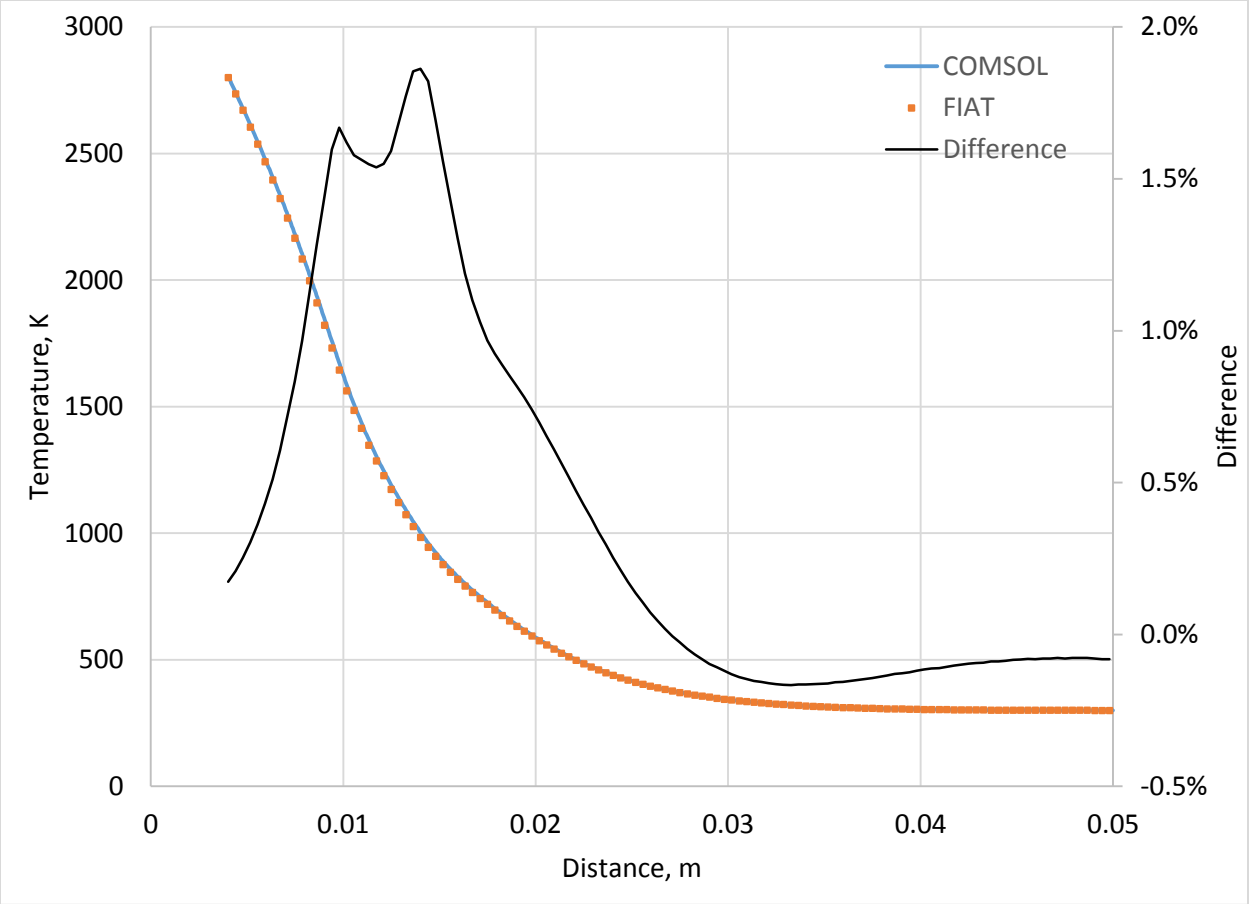

Figure 15. Predicted temperature profiles calculated by COMSOL and FIAT after 60-s exposure.

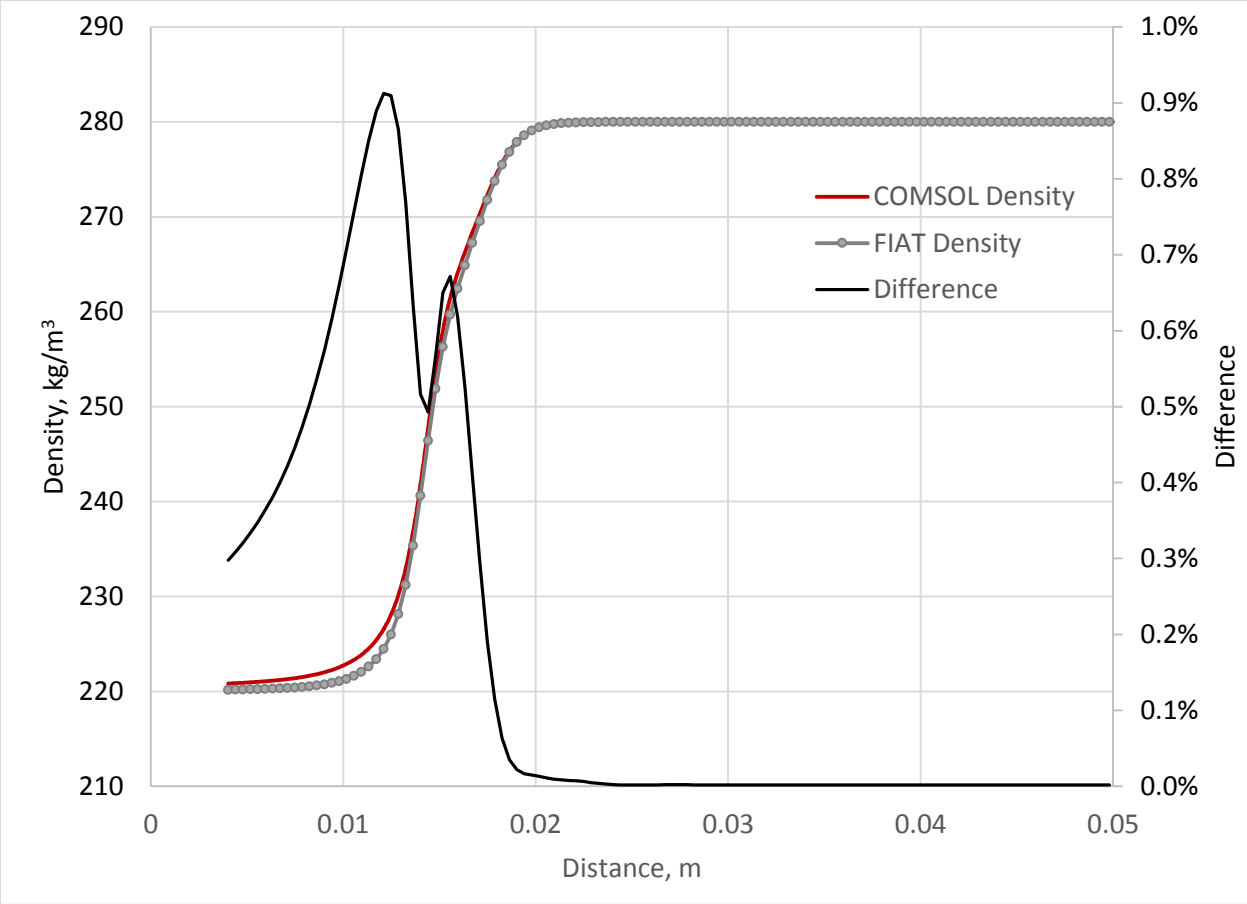

Figure 16. Predicted density profiles calculated by COMSOL and FIAT after 60-s exposure.

E. Example 5: Two-Dimensional Transient Analysis

The final problem considered here is the ablation of a cylindrical puck exposed to a high-intensity radiative input. The puck has a radius and thickness of 0.01 m. The front of the puck is subjected to a radiative input with a Gaussian intensity profile varying radially across the surface of the sample and equal to Eq. (35):

$$I = I_0 \exp(-C \cdot (1 - r/R)^2) \tag{35}$$

For this test, the value of I_0 is equal to 1.0×10^7 W/m^2 and the constant C was set equal to 5. The recovery enthalpy was set equal to 0 MJ/kg (room temperature air) with a heat transfer coefficient of 0.1 kg/m^2-s and the back and side faces of the puck were assumed to be adiabatic. Again, equal heat and mass transfer coefficients were assumed. An exposure time of 30 s was simulated. A grid of 40 by 40 rectangular cells was used. The cells were clustered closer to the center of the puck to increase resolution in the zone with the highest temperature and density variations. This problem is difficult due to the large grid deformations.

In this multi-dimensional calculation, it is assumed that the pyrolysis gas distribution in the material can be calculated from Poisson's equation, Eq. (36):

$$\nabla^2 \Phi = \frac{\partial \rho}{\partial t} \tag{36}$$

where Φ is the stream function such that the vector representing the pyrolysis gas flowrate is Eq. (37):

$$\dot{\boldsymbol{m}}_{\boldsymbol{g}} = \nabla\Phi \tag{37}$$

This assumption is justified if the flow is primarily dominated by viscous losses and the pressure drop is proportional to the local mass flux where the constant of proportionality is not dependent on the local conditions. The boundary conditions on Eq. (36) include a zero value for the stream function at the ablating surface and zero mass flux at all other boundaries. The simulation is initiated with the puck at room temperature, virgin density, and zero pyrolysis gas flow.

Figure 17 illustrates the evolution of the mesh and illustrates the mesh distribution at 0 and 30 s and shows the large deformation of the grid. Unlike some codes, the moving boundary algorithm does not change the number of mesh points as the solution progresses. The code, however, provides a remeshing feature that adjusts the mesh distribution as the solution progresses. For this case, a remeshing criteria based on the mesh distortion was used and the remeshing criteria adjusted the grid once during the solution.

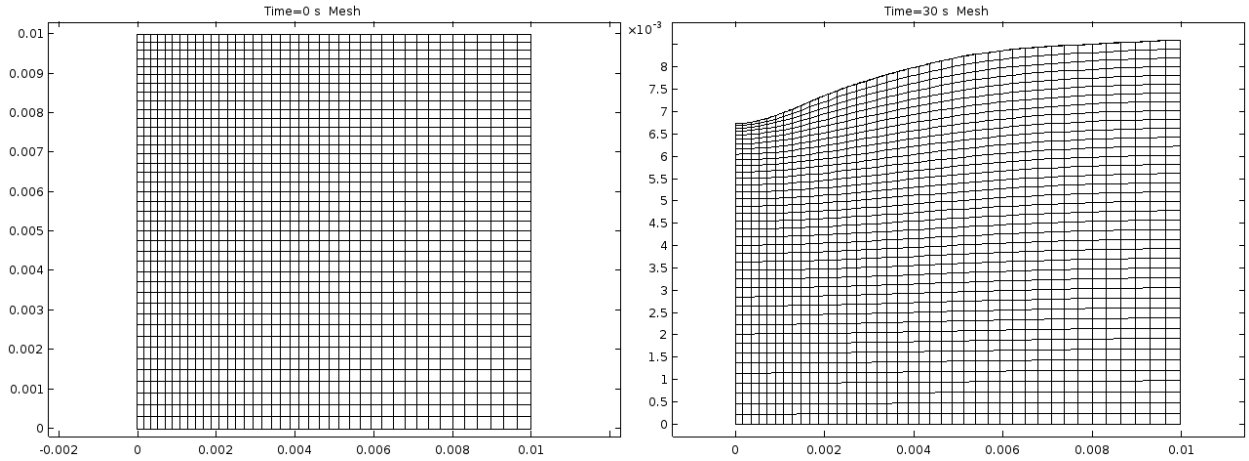

Figure 17. Two-dimensional mesh distribution at 0 and 30 s.

The temperature distribution as a function of time at 5, 10, 20, and 30 s is shown in Fig. 18. It can be seen that the temperature distribution develops fairly quickly and does not significantly change during the 30 s simulation time. The density distribution is shown similarly in Fig. 19. Here, clearly evident is the evolution of the pyrolysis zone through the material such that at 30 s, approximately 75% of the puck is fully pyrolyzed. Figure 20 illustrates the pyrolysis gas flowrate within the material again at 5, 10, 20, and 30 s. The pyrolysis gas flows primarily in the vertical (z) direction and orginates in the pyrolysis zone more clearly seen in Fig. 20. By 30 s, the material has almost completely pyrolyzed and the pyrolysis gas flow is reduced to nearly zero.

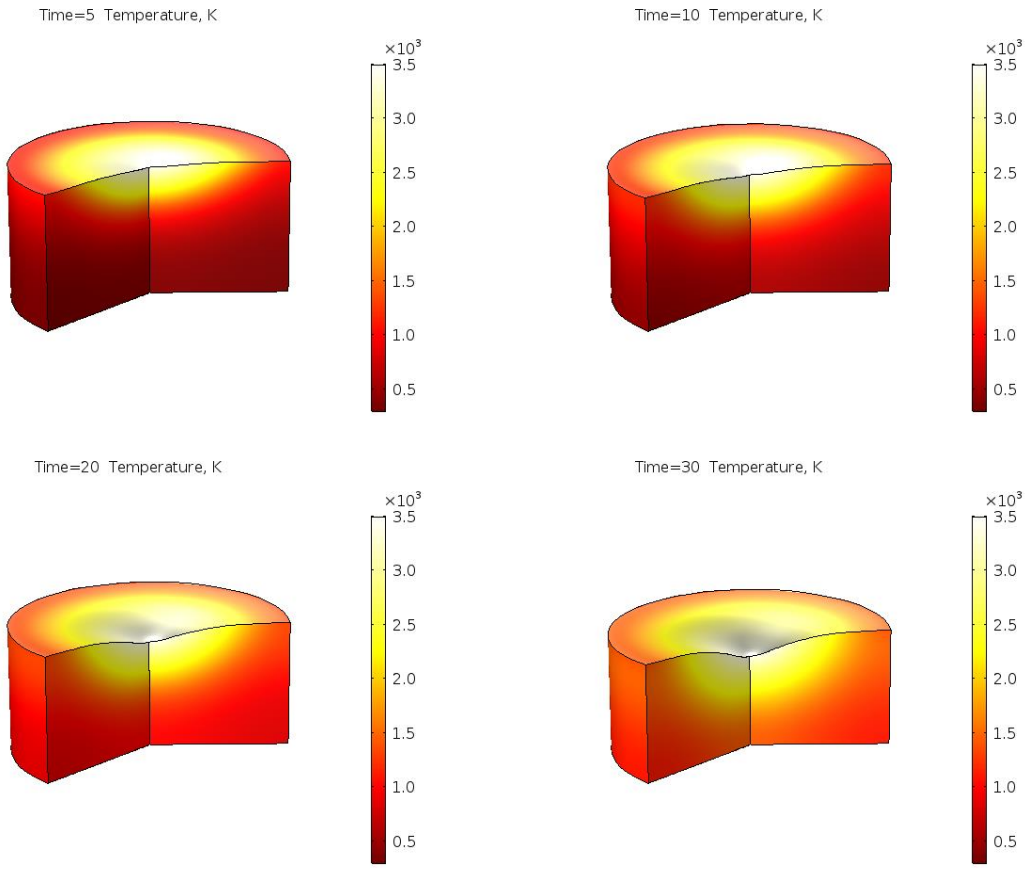

Figure 18. Two-dimensional temperature profile at 5, 10, 20, and 30 s.

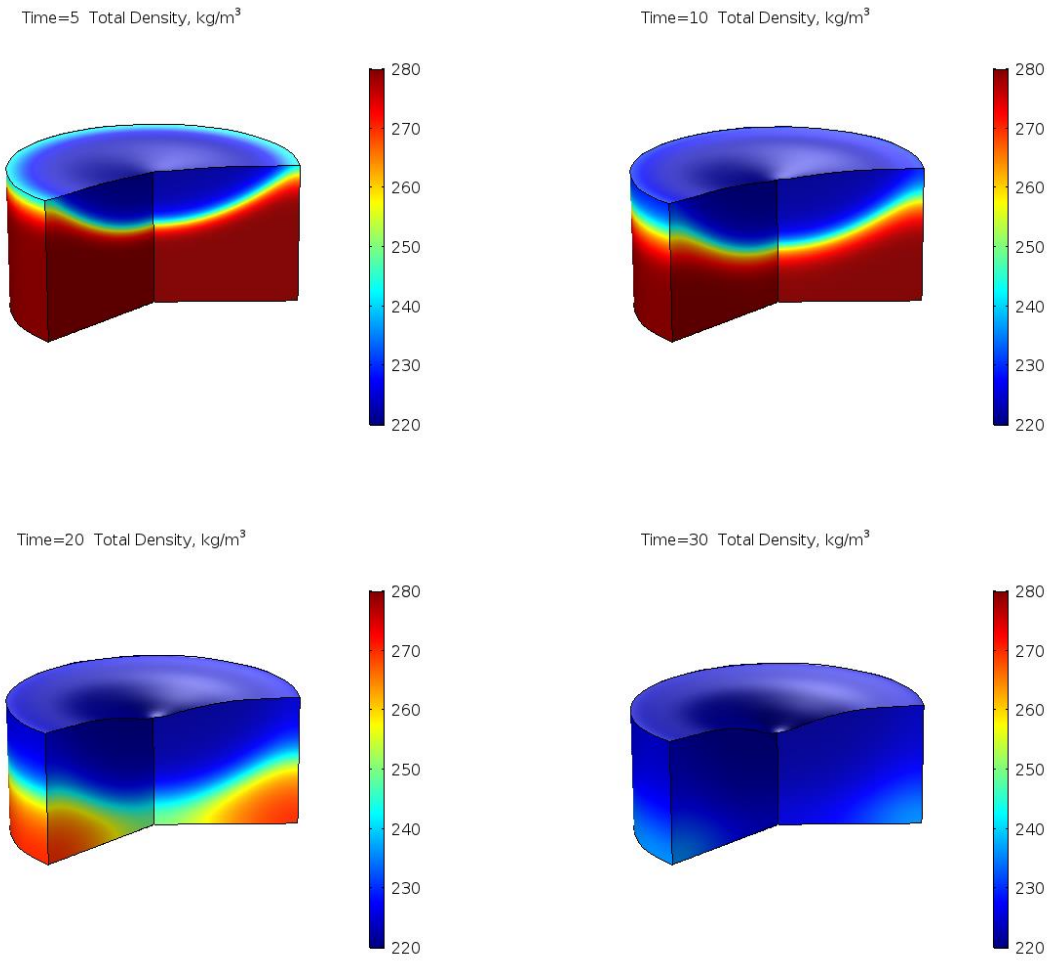

Figure 19. Two-dimensional total density profile at 5, 10, 20, and 30 s.

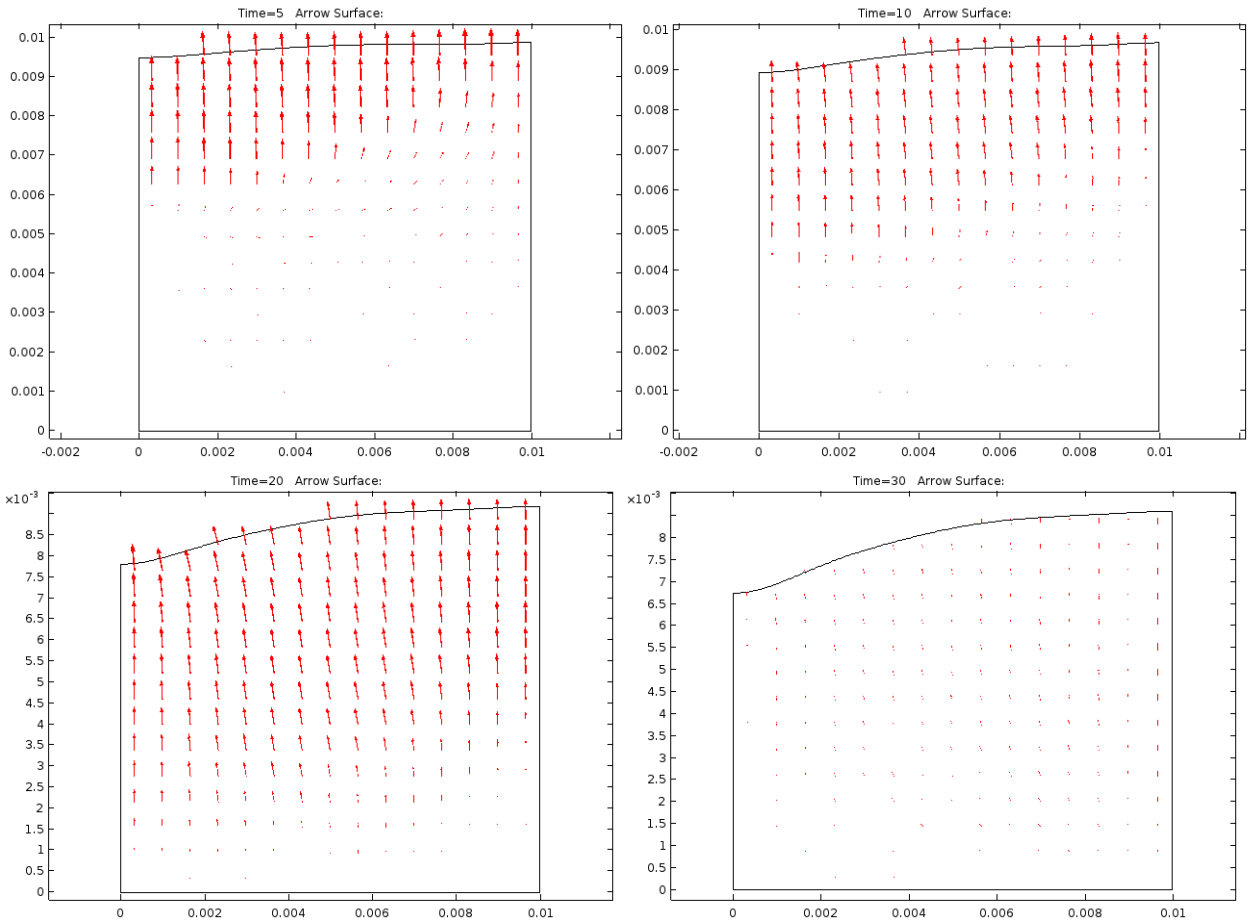

Figure 20. Pyrolysis gas flow at 5, 10, 20, and 30 s.

Figure 21 illustrates the computed surface profile after 30 s. The results from the 3-D solution are shown along with two other solution types. To provide a check on the model, the two-dimensional model was modified to suppress conduction in the radial direction and allow pyrolysis gas flow only in the vertical (z) direction. This result is shown as the Quasi-1D solution in Fig. 21. From this it can be seen that multi-dimensional conduction and pyrolysis gas flowrate effects are indeed significant. Radial conduction near the center of the sample significantly reduces the predicted recession. Also shown on the plot are the results of 20 one-dimensional solutions that, in theory, should agree with the Quasi-1D solution. The 1-D models used the local incident flux from the Gaussian distribution. Good agreement is obtained validating the model.

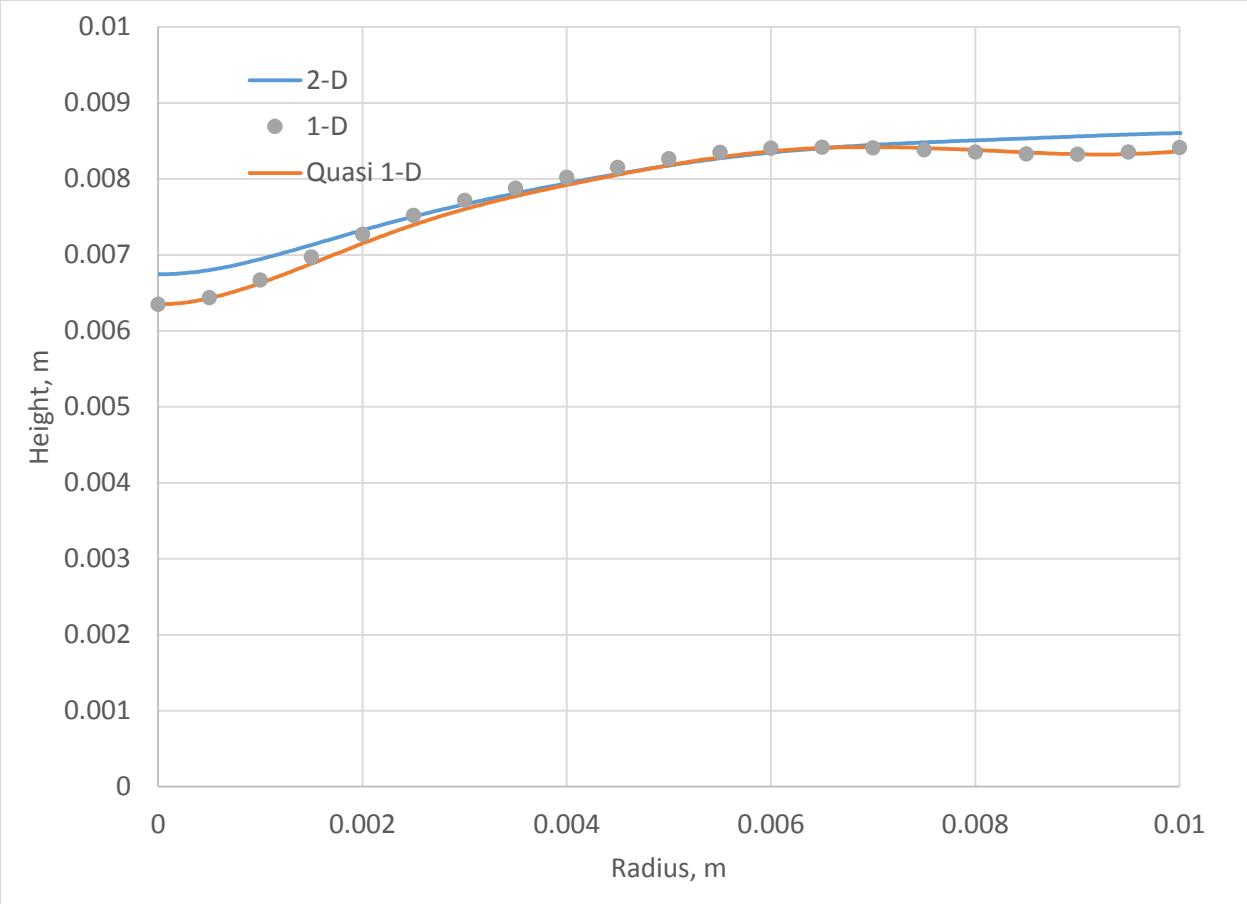

Figure 21. COMSOL solutions to the two-dimensional ablation problem showing the ablated surface profile at 30 s. Three types of solutions are shown: 1) Full two-dimensional (2-D), 2) two-dimensional solution with suppressed radial conductivity and pyrolysis gas flow only in the z (vertical direction) (Quasi 1-D), and 3) one-dimensional solutions (1-D).

V. Discussion

The results presented here demonstrate that COMSOL Multiphysics® provides solutions that match reasonably, if not nearly exactly, with other ablation tools. One of the primary advantages of the COMSOL tool is the integration of geometry modeling, mesh generation, post-processing, and a solution solver in a single, unified interface. The same program also has the capability of solving a variety of problems (thermogravimetric analysis, steady-state, transient ablation) in different geometries (rectangular and axisymmetric) and spatial dimensions (0-D, 1-D, 2-D, and 3-D) using a single interface. The extremely flexible capabilities of the code allow modifications and additions to ablation models to be easily incorporated into new applications that model structural and other phenomena. The COMSOL tool also offers the ability to perform multiple solutions for different values of specified parameters (parameter sweeps). The steady-state calculations for surface temperature and recession rate presented in "Example 2: Steady-State Ablation Analysis," were completely automated by the COMSOL program. Additionally, the COMSOL program also offers optimization capabilities that can be used to find the ideal design.

One of the main advantages of COMSOL is the ability to solve problems with multi-physical interactions. COMSOL includes computational fluid dynamics and structural capabilities with the requisite interfaces to couple these phenomenon together, so in principle it should be possible to couple the in-depth ablation analysis with external flow and structural modeling.

Finally, the user base for COMSOL is significant and growing rapidly. This means that the solution algorithms and accuracy of the code are stressed and subsequently verified by a large number of users. It is abundantly clear by using the code, that COMSOL Multiphysics® is a robust, well-written software application with tremendous potential and expanding capabilities with application to the design of TPS and spacecraft systems.

VI. Conclusions

The commercial finite element code COMSOL Multiphysics® (COMSOL, Inc., Burlington, Massachusetts) was used to model and analyze a pyrolyzing ablator composed of the simulated Theoretical Ablative Composite for Open Testing (TACOT) material. The results have been verified using a number of other computational tools, including the Fully Implicit Ablation and Thermal (FIAT) Response code, which is a well vetted ablation code. The work shows that COMSOL Multiphysics® is a suitable and advantageous tool for the analysis of pyrolyzing ablators.

Appendix
Theoretical Ablative Composite for Open Testing (TACOT) Material Properties

The material system used for the comparisons presented here is the Theoretical Ablative Composite for Open Testing (TACOT) model, which is an open, simulated pyrolyzing ablator that has been used a baseline test case for modeling ablation and comparing various predictive models (Ref. A1). All properties listed in this appendix are from Ref. A1.

Pertinent values for the decomposition constants for the three material components are summarized in Table A1.

Table A1. TACOT reaction rate constants and virgin and residual (char) densities.

$\Gamma = 0.5$, $\phi = 0.8$

Reaction	$\rho_{o,i}$	$\rho_{r,i}$	A_i	E_i/R	ψ_i	Initial reaction temperature
	(kg/m³)	(kg/m³)	sec^{-1}	(K)	(---)	(K)
A	300	0	1.20×10^{4}	8,556	3	333
B	900	600	4.48×10^{9}	20,440	3	556
C	1600	1600	0.00	0	0	5556

Components A and B comprise the resin; component C is the reinforcement. The resin decomposes but the reinforcement does not. The char yield of the material is equal to 78.57% (1100/1400 accounting for the component volume fractions). Under steady conditions, the ratio of char to pyrolysis gas is 3.66 (1100/300).

The values listed in Table A1 are for the solid composite components. The actual composite is 80% porous ($\phi = 0.8$), therefore the actual virgin and char composite density are only 20% of the individual constituents, resulting in a densities equal to 280 and 220 kg/m^3, respectively.

The elemental composition of the TACOT material is summarized in Table A2. The numbers in Table A2 are based on the reported pyrolysis mass fraction, the assumption that the reinforcement composition is 100% carbon, and the relative amounts of resin and reinforcement given in Table A1.

Table A2. Elemental mass fraction composition of the virgin and char material and the pyrolysis gas.

Element	Molecular weight, g/mol	Mass fraction, pyrolysis, %	Mass fraction, char, %	Mass fraction, virgin, %
Carbon	12.011	49.55	100.00	89.19
Hydrogen	1.00079	13.61	0.00	2.92
Oxygen	15.9994	36.84	0.00	7.90
Total		100.00	100.00	100.00

Surface thermochemistry relations for the TACOT material are available at several pressures. However, examples in this paper are conducted at a single pressure of 1 atm. Plots of the normalized char mass loss rate B'_c versus temperature at 1 atm for various values of the normalized pyrolysis mass loss rates B'_g are shown in Fig. A1. Similarly, the enthalpy versus temperature relationship is shown in Fig. A2.

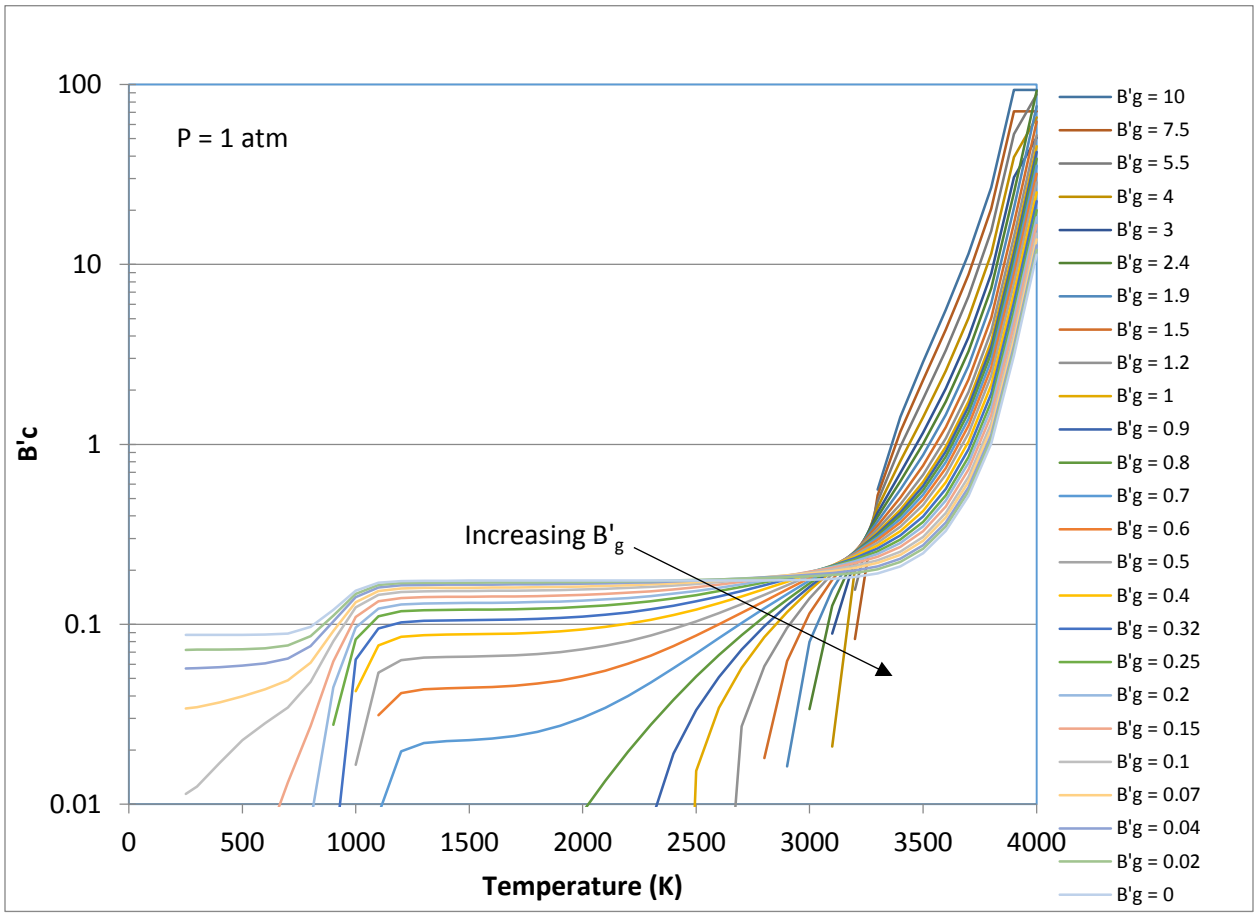

Figure A1. Plot of the normalized char mass loss rate B'_c versus temperature at 1 atm for various values of the normalized pyrolysis mass loss rate B'_g.

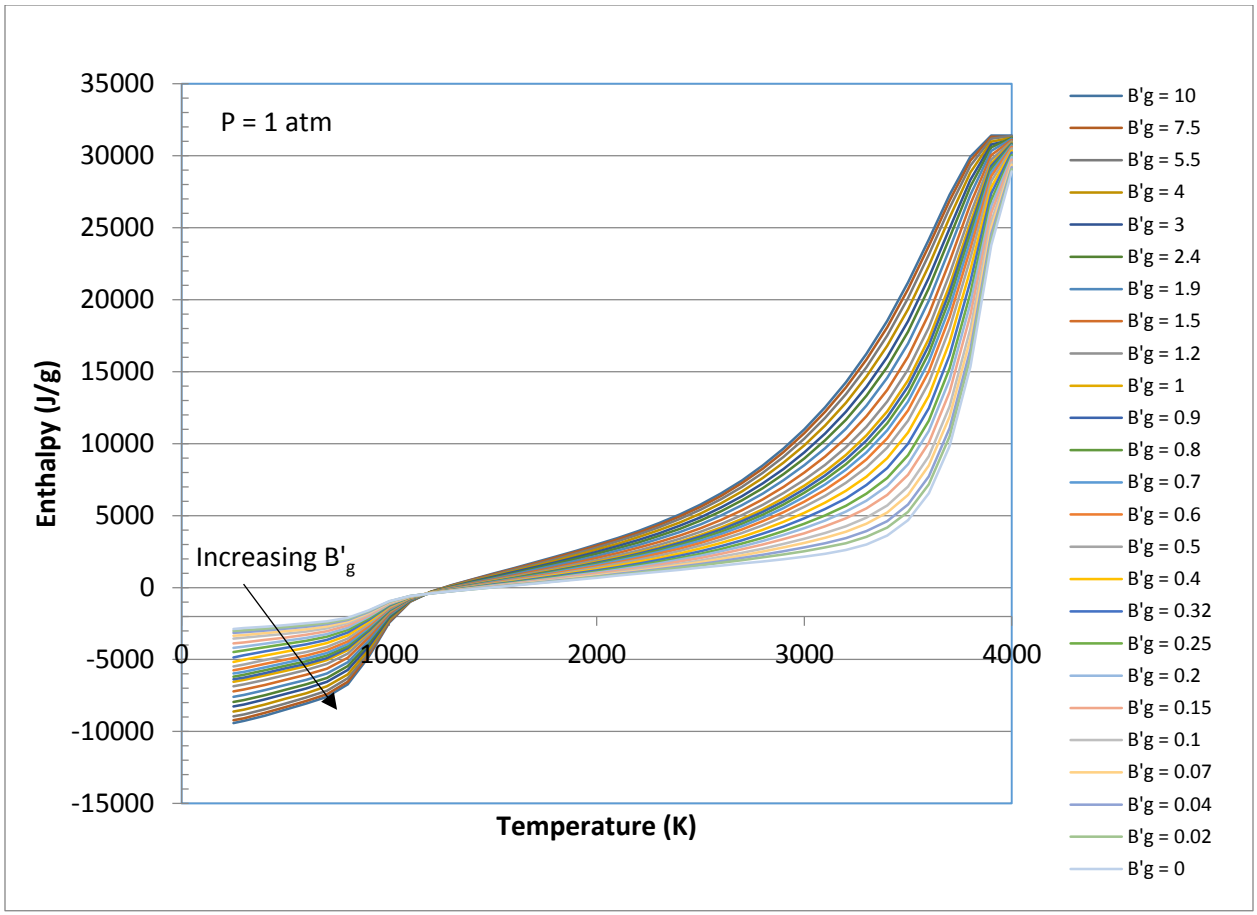

Figure A2. Plot of the gas phase surface enthalpy versus temperature at 1 atm for various values of the normalized pyrolysis mass loss rate B'_g.

Thermal conductivity and specific heat values as a function for the virgin and char are shown in Fig. A3. The TACOT material is assumed to be isotropic, therefore the thermal conductivity values are valid in all directions.

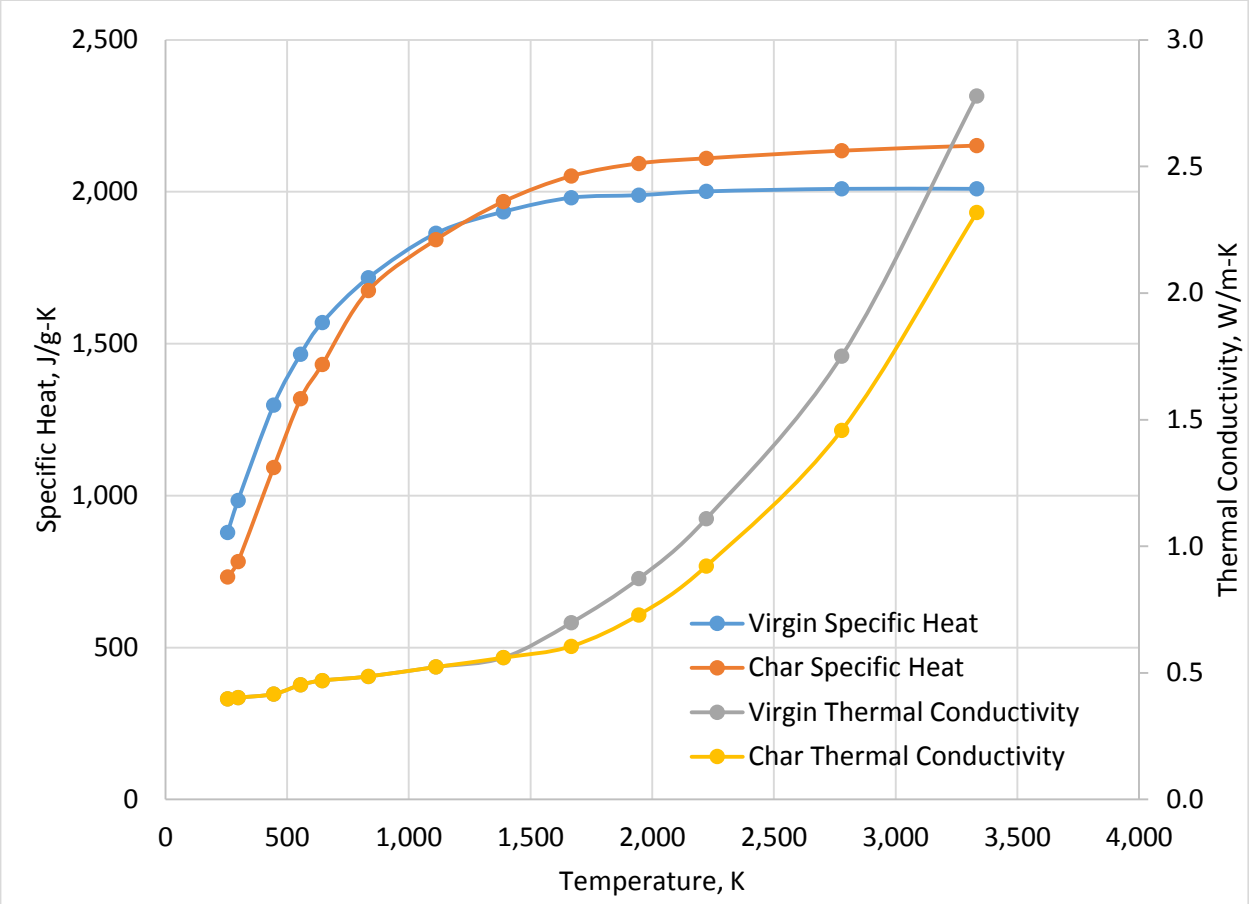

Figure A3. Specific heat values and thermal conductivity as a function of temperature for the virgin and char materials.

The local specific heat and thermal conductivity are formulated from the input temperature functions for both virgin material and char, $C_{p,v}$, $C_{p,c}$, k_v, and k_c. In partially-pyrolyzed zones ($\rho_c < \rho < \rho_v$), the specific heat and thermal conductivity is formulated with a special mixing rule, as shown in Eqs. (A1 and A2):

$$k = xk_v + (1-x)k_c \tag{A1}$$

$$C_p = xC_{p,v} + (1-x)C_{p,c} \tag{A2}$$

where the weighting variable x is based on the convenient fiction that partially-pyrolyzed material is a simple mixture of pure virgin material and pure char. The quantity x is defined as the mass fraction of pure virgin material in this imaginary mixture, which yields the correct local density as shown in Eq. (A3):

$$x = \frac{\rho_v}{\rho_v - \rho_c}\left(1 - \frac{\rho_c}{\rho}\right) \tag{A3}$$

The surface emissivity ε and absorptivity α are similarly defined as a combination of the virgin and char properties, as shown in Eqs. (A4) and (A5):

$$\varepsilon = x\varepsilon_v + (1-x)\varepsilon_c \tag{A4}$$

$$\alpha = x\alpha_v + (1 - x)\alpha_c \tag{A5}$$

For the TACOT material, the emissivity and absorptivity of the virgin material and char material are temperature-independent and each equal to 0.8 for the virgin material and 0.9 for the char material.

The virgin and char solid enthalpies are calculated based on the thermodynamic definition presented in Eq. (A6):

$$h = \int_{T_0}^{T} C_p dT + h_0 \tag{A6}$$

where h_0 is the enthalpy of formation at the reference temperature (taken to be 298.15 K). The enthalpies of formation for the char and virgin material are 0 and -857.1 kJ/kg, respectively. Plots of enthalpy versus temperature for the virgin and char solid are shown in Fig. A4.

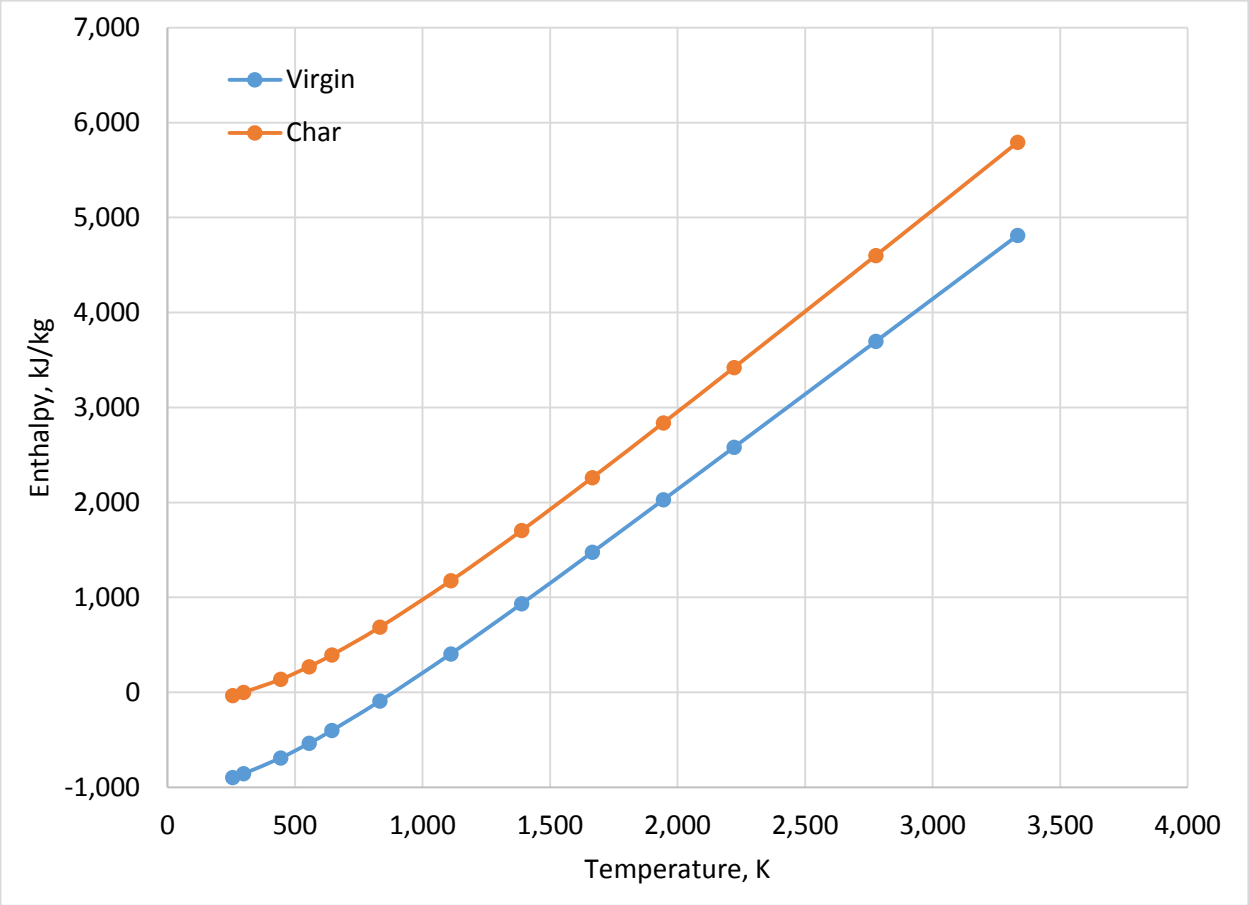

Figure A4. Solid enthalpies for virgin and char materials as function of temperature.

The pyrolysis gas enthalpy h_g is an input temperature and pressure-dependent function, Eq. (A7):

$$h_g = h_g(p, T) \tag{A7}$$

A plot of the pyrolysis gas enthalpy versus temperature for several pressures is shown in Fig. A5. Again, in this work, only tests cases at 1 atm were performed.

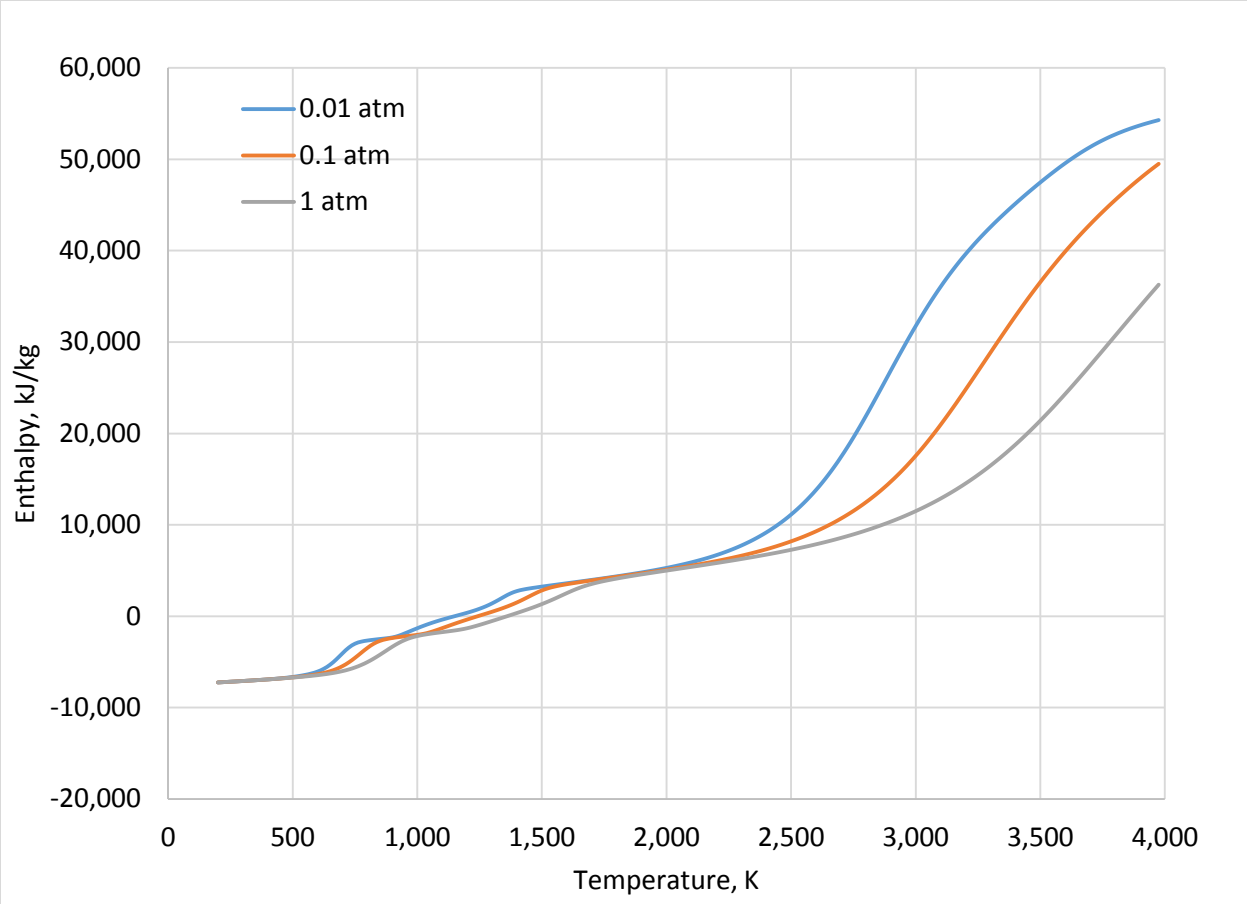

Figure A5. Pyrolysis gas enthalpy for the TACOT material as a function of temperature for pressures of 0.01, 0.1, and 1 atm.

References

[1]Kendall, R. M, Rindal, R. A., and Bartlett, E P., "A Multicomponent Boundary Layer Chemically Coupled to an Ablating Surface," *AIAA Journal*, Vol. 5., No. 6, 1967, pp. 1063-1071.

[2]Moyer, C. B., Anderson, L. W., and Dahm, T. J., *A Coupled Computer Code for the Transient Thermal Response and Ablation of Non-charring Heat Shields and Nose Tips*, NASA CR-1630, October 1970.

[3]Bunker, R. C., Maw, J. F., and Vogt, J. C, "A 2-D Axisymmetric Charring and Ablation Heat Transfer Computer Code," DTIC accession number ADP004977, 1984.

[4]Chen, Y.-K., and Milos, F. S., "Ablation and Thermal Response Program for Spacecraft Heatshield Analysis," *Journal of Spacecraft and Rockets*, Vol. 36, No. 3, 1999, pp. 475-483.

[5]Milos, F. S., and Chen, Y.-K., "Two-Dimensional Ablation, Thermal Response, and Sizing Program for Pyrolyzing Ablators," *Journal of Spacecraft and Rockets*, Vol.46, No. 6, 2009, pp. 1089-1099, DOI: 10.2514/1.36575.

[6]Chen, Y.-K., and Milos, F. S., "Three-Dimensional Ablation and Thermal Response Simulation System," AIAA-2005-5064, 2005.

[7]Chen, Y.-K., Milos, F. S., and Gokçen, T., "Validation of a Three-Dimensional Ablation and Thermal Response Simulation Code," AIAA-2010-4645, 2005.

[8]Blackwell, B. F., "Numerical prediction of a 1-D Ablation Using a Finite Control Volume Procedure with Exponential Differencing." AIAA-88-0085, 1988.

[9]Blackwell, B. F., and Hogan, R. E., "One-Dimensional Ablation Using Landau Transformation and Finite Control Volume Procedure," *Journal of Thermophysics and Heat Transfer*, Vol. 8, No. 2, 1994, pp. 282-287.

[10]Hogan, R. E., Blackwell, B. F., and Cochran, R. J., "Application of Moving Grid Control Volume Finite Element Method to Ablation Problems," *Journal of Thermophysics and Heat Transfer*, Vol. 10, No. 2, 1996, pp. 312-319.

[11]Chin, J. H., "Finite Element Analysis for Conduction and Ablation Moving Boundary", AIAA-80-1488, 1980.

[12]Bhatia, A., and Roy, S., "Modeling the Motion of Pyrolysis Gas Through Charring Ablating Material Using Discontinuous Galerkin Finite Elements," AIAA-2010-982, 2010.

[13]Dec, J. A., and Braun, R. A., "Three-Dimensional Finite Element Ablative Thermal Response and Design of Thermal Protection Systems," *Journal of Spacecraft and Rockets*, Vol. 50, No. 4, 2013, pp. 725-734, DOI: 10.2514/1.A32313.

[14]Howard, M. A., and Blackwell, B. F., "A Multi-Dimensional Finite Element Based Solver for Decomposing and Non-decomposing Thermal Protection Systems," AIAA 2015-2506, 2015.

[15]Lachaud, J., and Mansour, N. N., "Porous-Material Analysis Toolbox Based on OpenFOAM and Applications," *Journal of Thermophysics and Heat Transfer*, Vol. 28, No. 2, 2104, pp. 191-202.

[16]Amar, A. J., Oliver, A. B., Kirk, B. S., Salazar, G., and Droba, J., "Overview of the CHarring Ablator Response (*CHAR*) Code," AIAA-2016-3385, 2016.

[17]Santos, J. A., Beck, R. A. S., and Risch, T. K., "Thermal Modeling of In-Depth Thermocouple Response in Ablative Heat Shield Materials," AIAA-2008-4134, 2008.

[18]Carandente, V., Scigliano, R., De Simone, V., Del Vecchio, A., and Gardi, R., "A Finite Element Approach for the Design of Innovative Ablative Materials for Space Applications," 8th European Symposium on Aerothermodynamics for Space Vehicles, 2 - 6 March 2015, IST Congress Centre, Lisbon, Portugal.

[19]Wertheimer, T. B., and Laturelle F., "Thermal Decomposition Analysis of Rocket Motors and other Thermal Protection Systems Using MSC.Marc-ATAS," 14th Annual Thermal and Fluid Analysis Workshop (TFAWS), August 18-22, 2003.

[20]Tabiei, A., and Sockalingam, S., "Multiphysics Coupled Fluid/Thermal/Structural Simulation for Hypersonic Reentry Vehicles," *Journal Of Aerospace Engineering*, April 2012, pp. 273-281.

[21]Wang, Y., and Zhupanska, O. I., "Thermal Ablation in Fiber-Reinforced Composite Laminates Subjected to Continuing Lightning Current," AIAA-2016-0986, 2016.

[22]Siemens PLF Software, "LMS Samtech Realistic Virtual Simulation; LMS Samcef Amaryllis," https://www.plm.automation.siemens.com/en_us/products/lms/samtech/samcef-solver-suite/amaryllis.shtml [cited 29 March 2017].

[23]Risch, T., and Kostyk, C., "HTV-2 Carbon Kinetics Sensitivity Analysis," 39th Annual Conference on Composites Materials and Structures, 2015. Available from the DARPA Tactical Technical Office, 675 N. Randolph Street, Arlington, VA 22203.

[24]Risch, T., and Kostyk, C., "HTV-2 2-D Aeroshell Thermal Analysis," 40th Annual Conference on Composites Materials and Structures, January 25-29, 2016. Available from the DARPA Tactical Technical Office, 675 N. Randolph Street, Arlington, VA 22203.

[25]Goldstein, H. E., "Kinetics of Nylon and Phenolic Pyrolysis," LMSC-667876, 1965.

[26]Bird, R. B., Stewart, W. E., and Lightfoot, E. N., *Transport Phenomena*, John Wiley & Sons, Inc., 1960, pp. 658-668.

[A1]Lachaud, J., Martin, A., Cozmuta, I., and Laub, B., "Test Case Series 1," 4th AF/SNL/NASA Ablation Workshop, Albuquerque, New Mexico, 2011.